Quality Controlling Surfzone Acoustic Doppler Velocimeter Observations to Estimate the Turbulent Dissipation Rate

FALK FEDDERSEN[1]

[1]*Scripps Institution of Oceanography, La Jolla, California*

Submitted, *Journal of Atmospheric and Oceanic Technology,* XXX-XX-XXXX

March 15, 2010

Corresponding author address:

F. Feddersen, Scripps Institution of Oceanography, 9500 Gilman Dr., La Jolla CA 92093-0209

Report Documentation Page

Form Approved
OMB No. 0704-0188

1. REPORT DATE	2. REPORT TYPE	3. DATES COVERED
15 MAR 2010		**00-00-2010 to 00-00-2010**

4. TITLE AND SUBTITLE	5a. CONTRACT NUMBER
Quality Controlling Surfzone Acoustic Doppler Velocimeter Observations to Estimate the Turbulent Dissipation Rate	5b. GRANT NUMBER
	5c. PROGRAM ELEMENT NUMBER
6. AUTHOR(S)	5d. PROJECT NUMBER
	5e. TASK NUMBER
	5f. WORK UNIT NUMBER
7. PERFORMING ORGANIZATION NAME(S) AND ADDRESS(ES) **Scripps Institution of Oceanography,9500 Gilman Dr,La Jolla,CA,92093-0209**	8. PERFORMING ORGANIZATION REPORT NUMBER
9. SPONSORING/MONITORING AGENCY NAME(S) AND ADDRESS(ES)	10. SPONSOR/MONITOR'S ACRONYM(S)
	11. SPONSOR/MONITOR'S REPORT NUMBER(S)

12. DISTRIBUTION/AVAILABILITY STATEMENT
Approved for public release; distribution unlimited

13. SUPPLEMENTARY NOTES

14. ABSTRACT

15. SUBJECT TERMS

16. SECURITY CLASSIFICATION OF:			17. LIMITATION OF ABSTRACT	18. NUMBER OF PAGES	19a. NAME OF RESPONSIBLE PERSON
a. REPORT **unclassified**	b. ABSTRACT **unclassified**	c. THIS PAGE **unclassified**	**Same as Report (SAR)**	**46**	

ABSTRACT

High-quality measurements of the turbulent dissipation rate $\bar{\epsilon}$ are required to diagnose field surfzone turbulence budgets. Quality control (QC) methods are presented for estimating surfzone $\bar{\epsilon}$ with Acoustic Doppler Velocimeter (ADV) data. Bad ADV velocity data points are diagnosed with both the ADV signal-strength (SS) and correlation (CORR). The fraction of bad SS data points (δ_{SS}) depends inversely upon the wave-amplitude normalized transducer distance below the mean sea-surface. The fraction of bad CORR data points δ_{CORR} can be elevated when δ_{SS} is low. The δ_{CORR} depends inversely upon the wave-amplitude normalized sensing volume distance below the mean sea-surface and also increases with increased wave-breaking, consistent with turbulence and bubble induced Doppler noise. Velocity spectra derived from both "patched" and "interpolated" time series is used to estimate $\bar{\epsilon}$. Two QC tests, based upon the properties of a turbulent inertial-subrange, are used to reject bad $\bar{\epsilon}$ data runs. The first test checks that the vertical velocity spectrum's power-law exponent is near $-5/3$. The second test checks that a ratio R of horizontal and vertical velocity spectra is near one. Over all δ_{CORR}, 70% of patched and interpolated data runs pass these tests. However, for larger $\delta_{\mathrm{CORR}} > 0.1$ (locations higher in the water column) 50% more patched than interpolated data runs pass the QC tests. Previous QC methods designed for wave studies are not appropriate for $\bar{\epsilon}$ QC. The results suggest that $\bar{\epsilon}$ can be consistently estimated over the lower 60% of the water column and > 0.1 m above the bed within a saturated surfzone.

1. Introduction

Surfzone turbulence vertically mixes momentum, tracers, and sediment. High quality surfzone turbulence measurements are critical to diagnosing surfzone turbulence energetics. Measurements of turbulent dissipation rate ϵ, often used to study oceanic turbulence (*e.g.,* Terray et al. 1996; Gerbi et al. 2009), are sparse within the surfzone. Measuring surfzone turbulence is challenging because breaking waves and strong currents exert powerful forces on instruments, the water and sea-bed both vary substantially, and high levels of turbulence, bubbles and suspended sediment corrupt velocity measurements.

Acoustic Doppler Velocimeters (ADV) measures 3-components of velocity, at high sampling rates, by measuring the Doppler shift of returned acoustic pulses (Sontek 2004). ADVs have been used to study waves (*e.g.,* Thomson et al. 2007) and mean circulation (*e.g.,* Apotsos et al. 2008) in the surfzone and nearshore. The ADV accurately measures Reynolds stresses and turbulent velocity spectra in laboratory flumes (Voulgaris and Trowbridge 2001). ADVs have also been used to study turbulence in a laboratory surfzone (*e.g.,* Scott et al. 2005), in estuarine and coastal (*e.g.,* Kim et al. 2000) environments, and in field surfzone (Bryan et al. 2003) and swash-zone (Raubenheimber et al. 2004).

The ADV sensor also returns the backscattered acoustic signal-strength (SS) and the correlation (CORR) of successive pings (*e.g.,* Zedel et al. 1996). Both SS and CORR are used to diagnose ADV data quality. Surfzone ADV velocity measurements can be noisy with significant amounts of bad data (Elgar et al. 2001). The signal strength (SS) depends upon the density of scatterers (*e.g.,* Lohrmann et al. 1994). With insufficient scatterers, SS is low and the velocity signal is unreliable. Within the surfzone, there is generally no shortage of scatterers (*e.g.,* bubbles and suspended sediment). Low SS also occurs when the ADV sensor is exposed out of the water (*i.e.,* above water level) or when the scatterer density is so high that the acoustic signal is absorbed or scattered (*e.g.,* Elgar et al. 2005). Along beam correlation (CORR), the coherence between the Doppler shift observed with successive pings, is low (Cabrera et al. 1987) when scatterers leave

the sampling volume between pings or when velocity fluctuates or is sheared within the sample volume (Lhermitte and Lemmin 1994). Low CORR lead to inaccurate velocity estimates (Zedel et al. 1996). Low CORR also occurs in the presence of significant number of bubbles (Mori et al. 2007), and when the ADV sensing volume is too close to the bed (Martin et al. 2002; Elgar et al. 2005), generally one sample volume width above the bed (Raubenheimber et al. 2004).

Elgar et al. (2005) suggests flagging data points as bad when the signal-strength $\mathrm{SS} < \gamma_{\mathrm{SS}}$ (SS is an 8-bit count 0–255) from any of the Sontek Ocean 3 ADV acoustic beams. The signal-strength cutoff $\gamma_{\mathrm{SS}} = 100$ was chosen by examination of surfzone data during times when the probe was known to be both in and out of the water. This γ_{SS} is specific to the particular Sontek ADV sensor and other sensors may give different γ_{SS} (B. Raubenheimer, personal communication). Elgar et al. (2005) reject an entire data run if the fraction of bad SS data points $\delta_{\mathrm{SS}} > 0.008$. This empirical criteria is conservative, assuring that little bad data passes.

The ADV correlation (CORR) signal (ranging from 0–1.0) also is used to diagnose data quality (Zedel et al. 1996; Sontek 2004). To mark data points as bad, Elgar et al. (2005) proposed a correlation threshold γ_{CORR} of

$$\gamma_{\mathrm{CORR}} = 0.3 + 0.4\sqrt{f_s/f_{\max}} \tag{1}$$

where f_s is the sample frequency and $f_{\max}$ is the maximum ADV sampling frequency ($f_{\max} = 25$ Hz for the Sontek Ocean ADV). The upper (0.7) and lower (0.3) γ_{CORR} limits are based on Sontek (2004) estimates for full sampling and mean flow, respectively. Data points where the CORR $< \gamma_{\mathrm{CORR}}$ on any of the three beams are marked bad. Unlike the δ_{SS} rejection criteria, Elgar et al. (2005) did not propose a data-run rejection criteria based upon the fraction of bad CORR points δ_{CORR}. Instead, two QC tests, based upon the expected properties of the surface gravity wave field in the sea-swell band, are used to reject data runs. The first test statistic is the pressure p to (interpolated-) cross-shore velocity (u) coherence $\bar{\mathrm{C}}_{pu}$, and the second statistic is based upon the ratio of pressure to horizontal velocity variance (*i.e.,* Z^2, Guza and Thornton 1980). Thresholds for Z^2 and $\bar{\mathrm{C}}_{pu}$ tests were selected empirically. A large δ_{CORR} usually indicated that a data run

would not pass the Z^2 and $\bar{\mathrm{C}}_{pu}$ tests, but some cases with large δ_{CORR} (up to $\delta_{\mathrm{CORR}} = 0.5$) did pass these tests (Elgar et al. 2005). This ADV QC methodology works well for wave and mean current studies (*i.e.,* at frequencies < 0.3 Hz), but is constrained by the requirement of a co-located and synchronized pressure measurement.

Turbulent dissipation rate ϵ estimates depend crucially upon the high frequency (> 1 Hz) component of the velocity spectrum rather than on sea-swell band frequencies (~ 0.1 Hz). In nearshore and surfzone field studies of ϵ, ADV QC methods vary. In 4.5 m mean water depth, a location only occasionally within the surfzone, ADV measurements 1 m above the bed were used to estimate ϵ (Trowbridge and Elgar 2001). ADV data quality control used the manufacturer's suggested γ_{CORR}; δ_{CORR} levels, and bad data interpolation were not discussed. Instead, assuming unidirectional and pure shallow-water wave-orbital motions with a steady current, Trowbridge and Elgar (2001) showed that within an inertial subrange (at high frequencies with no instrument noise)

$$\frac{(12/21)(P_{uu}(f) + P_{vv}(f))}{P_{ww}(f)} = 1, \tag{2}$$

where P_{uu}, P_{vv}, and P_{ww} are the cross-shore, alongshore and vertical velocity spectra, respectively and f is frequency. The quality of ϵ estimates was ensured by checking that a ratio R, based upon the left-hand-side of (2), was near one. Although the assumptions used to derive (2) are not generally valid within a natural surfzone, on average $R \approx 0.8$ was observed, suggesting that a turbulent inertial subrange was present and the resulting $\epsilon \lesssim 10^{-4}\ \mathrm{m^2\,s^{-3}}$ (Trowbridge and Elgar 2001).

In a study of the ϵ vertical structure seaward of the surfzone (no depth-limited wave breaking) in 3.5 m mean water depth (Feddersen et al. 2007), the SS and CORR (1) thresholds (Elgar et al. 2005) were applied to data from a vertical stack of 3 ADVs. No co-located pressure sensor was present and thus the Z^2 and $\bar{\mathrm{C}}_{pu}$ tests (Elgar et al. 2005) could not be applied. For all ADV data runs, the maximum $\delta_{\mathrm{CORR}} = 0.026$, and δ_{CORR} was typically much less. Data flagged as bad was interpolated following Elgar et al. (2005), and the resulting R varied between 0.8–1.5, and

ϵ varied between 10^{-5}-3×10^{-4} $\mathrm{m^2\,s^{-3}}$. However, these observations did not reach far up in the water column as $z'/H_{\mathrm{sig}} \geq 1$ (z' is the ADV distance below the mean sea-surface and H_{sig} is the significant wave height).

In an study of turbulent energetics with white-capping wave breaking in 16 m water depth (Gerbi et al. 2009), data runs with large vertical velocities or the ADV sensor too close to the surface (*i.e.,* $z'/H_{\mathrm{sig}} < 2$) were rejected, and the resulting $\epsilon \lesssim 10^{-5}$ $\mathrm{m^2\,s^{-3}}$. In a shallow estuary (1.5–3.5 m depth) study (Jones and Monismith 2008) of the ϵ vertical structure with whitecapping wind-waves (H_{sig} between 0.1–0.6 m), the ADV velocity QC methods were not specified. Estimates of ϵ were rejected if the vertical velocity spectrum was not consistent with a $-5/3$ power law over some frequency range. Measurements were reported relatively high up in the water column with z'/H_{sig} as small as 0.3 and z/h (where z is height above the bed and h is the mean water depth) as large as 0.9. The resulting ϵ was generally $\lesssim 10^{-4}$ $\mathrm{m^2\,s^{-3}}$ but occasionally was as large as 10^{-3} $\mathrm{m^2\,s^{-3}}$ high in the water column.

In a study of surfzone ϵ in < 3 m depths and with incident $H_{\mathrm{sig}} < 0.6$ m (Bryan et al. 2003), Sontek Ocean ADV data points with SS and CORR below the $\gamma_{\mathrm{SS}} = 77$ counts and $\gamma_{\mathrm{CORR}} = 0.7$ were marked as bad. Data runs were rejected if the fraction of total bad data points > 0.1, resulting in 62 of 194 data runs being discarded. The data interpolation method was not specified. Data runs were additionally rejected if the best-fit velocity spectra power-law was not near $-5/3$. The resulting ϵ varied between 10^{-5}–$10^{-3}\mathrm{m^2\,s^{-3}}$. Some retained data runs were relatively high up in the water column, at time exceeding $z/h > 0.7$.

In a swash-zone turbulence study (Raubenheimber et al. 2004), two vertical stacks of (two-velocity component) ADVs were deployed in 5 cm and 25 cm mean water depth. At the 25 cm location, the ADV was considered submerged (from the SS signal) most (98%) of the time. At the 5 cm location, only 25% of the data runs were considered as submerged. Bad data points were removed following Elgar et al. (2005). Data runs considered submerged rarely had $\delta_{\mathrm{CORR}} > 0.03$. Velocity spectra were calculated from the Fourier transform of the velocity auto-covariance,

precluding the need for data-gap interpolation, but perhaps biasing the spectra estimates. The turbulent dissipation rate ϵ was estimated from the high-frequency spectra following Trowbridge and Elgar (2001). The observed ϵ were the largest oceanic ϵ ever reported, up to $10^{-1}\ \mathrm{m^2\,s^{-3}}$, and were an order of magnitude larger than the combined shear production and depth-normalized breaking wave energy flux gradient (Raubenheimber et al. 2004).

Here, surfzone and nearshore ADV data are used to examine and develop quality control methodology for estimating surfzone ϵ. This process also should be applicable to open-ocean air-sea boundary ϵ studies. The surfzone and nearshore field ADV observations from the HB06 field experiment (Huntington Beach CA, Fall 2006) are described in Section 2. Bad ADV velocity data points are identified (Elgar et al. 2005) with both the ADV signal-strength (SS) and correlation (CORR) signals (Section 3). The fraction of bad SS data points δ_{SS} is a function of the (wave-amplitude) normalized ADV transducer depth below the surface. The bad-SS data gap statistics are used to assist in identifying a δ_{SS} cutoff to reject bad-SS data runs. The fraction of bad CORR points δ_{CORR} can be large even with small δ_{SS}. The resulting δ_{CORR} is related to both the sensing volume distance below the surface and the wave energy-flux gradient, consistent with turbulence- and bubble-induced Doppler noise within the sensing volume.

The method for estimating ϵ, the QC tests, and their application are described in Section 4. The two QC tests are based upon the properties of the turbulent inertial-subrange. Velocity spectra are calculated from "patched" and "interpolated" time-series. At smaller δ_{CORR} (< 0.1), patching and interpolation give similar results. At higher δ_{CORR}, patched data runs are more often consistent with an inertial subrange, and some data runs pass with δ_{CORR} as high as 0.4. The implications of the ϵ QC method are discussed in Section 5. The interpolated ϵ estimates are biased low relative to patched ϵ estimates. Previous QC methods designed for wave studies are shown to be inappropriate for $\bar{\epsilon}$ QC. Surfzone ϵ estimates can be consistently made at about $1.5\times$ wave amplitude below the mean sea-surface, corresponding to the lower 60% of the water column in a saturated surfzone. The results are summarized in Section 6.

2. The HB06 Surfzone ADV Observations

a. HB06 Instrumentation and Processing

FIG. 1

Surfzone field observations were collected during Fall 2006 at Huntington Beach CA State Park (lat: 33.636 N, lon: -117.969 E) as part of the HB06 experiment (Spydell et al. 2009; Clark et al. 2010; Omand et al. 2010). A cross-shore transect of six instrumented frames was deployed spanning 160 m from near the shoreline out to 4 m mean water depth (Fig. 1). An additional deployed instrumented frame (between instruments 1–2) was often buried and observations from it are not included here. At each instrument location, the vertical coordinate z is positive upward with $z = 0$ m at the bed. The cross-shore coordinate x is positive offshore. The instrument frames were leveled with possible orientation errors of $\pm 3^{\circ}$. The tide range was approximately ± 1 m. Data was collected for 800 hours from 14 September to 17 October 2006.

Each instrumented frame had a buried pressure (p) sensor and mounted downward looking 5 MHz Sontek Ocean Probe ADV (Sontek 2004) with synchronized data collection sampled at 8 Hz. Vertical instrument locations were GPS measured to within a few cm relative to mean sea level. The ADV measures 3 components of velocity (u, v, and w) aligned with the coordinate system. The velocity range was set to $\pm 5\ \mathrm{m\,s^{-1}}$, and velocities beyond this range (*i.e.,* phase wrapping) were not observed. In addition, the ADV returns signal-strength (SS) and correlation (CORR) on each of the 3 beams. Both SS and CORR are given as an unsigned byte (0-255 counts) and CORR is normalized to between 0–1.0. In each hourly data run, the ADV sampled 24,578 data points (51.2 min or 3072 s) and subsequently went into bottom finding mode for the remainder of the hour to estimate ADV transducer height above the sea-bed (z_{tr}) and bed location (relative to mean sea level).

From each pressure sensor, the mean sea surface location, mean water depth h, and sea-surface elevation spectra ($P_{\eta\eta}$) were estimated hourly. These calculations are independent of

the co-located ADV velocity data. Pressure spectra from buried sensors were adjusted following Raubenheimber et al. (1998). From the spectra, significant wave height $H_{\rm sig}$ is calculated over both sea-swell (0.03–0.3 Hz, $H^{\rm ss}_{\rm sig}$) and infragravity (0.003-0.03 Hz, $H^{\rm ig}_{\rm sig}$) frequency bands The total (sea-swell and infragravity bands) significant wave amplitude $a_{\rm sig}$ is given by $a_{\rm sig} = ((H^{\rm ss}_{\rm sig})^2 + (H^{\rm ig}_{\rm sig})^2)^{1/2}/2$. During the experiment, the incident $H^{\rm ss}_{\rm sig}$ varied between 0.5–1.4 m.

The (downward looking) ADV sensing volume vertical location $z_{\rm adv}$ is 0.18 m below the transducer location $z_{\rm tr}$ (*i.e.,* $z_{\rm tr} = z_{\rm adv} + 0.18$ m). The ADV sensing volume is a approximately $(0.01\ {\rm m})^3$) cylinder (Sontek 2004). During the deployment the sea-bed eroded and accreted and the ADVs were occasionally raised or lowered on the frames. At instruments 1–3, $z_{\rm adv}$ varied between 0–0.4 m, and at instruments 4–6, $z_{\rm adv}$ varied between 0.5–0.8 m. Data runs with sensing volume too close to the bed ($z_{\rm adv} \leq 0.03$ m) are rejected. The distance below the mean sea-surface of the sensing volume $z'_{\rm adv}$ and transducer ($z'_{\rm tr}$) is given by $z'_{\rm adv} = h - z_{\rm adv}$ and $z'_{\rm tr} = h - z_{\rm tr}$, respectively. Both $z'_{\rm adv}$ and $z'_{\rm tr}$ are relevant because when the transducer of a downward looking ADV is exposed out of the water the acoustic path is blocked even if the sensing volume remains submerged. For an upward looking ADV this is not a concern as the sensing volume location would be exposed first. For a horizontally mounted ADV $z_{\rm tr} = z_{\rm adv}$.

b. Example of ADV Data

FIG. 2

The challenges in using surfzone ADV data to estimate (high frequency) turbulence parameters are illustrated with a short (160 s) time series of ADV data (Fig. 2). In general, the vertical velocities are small ($|w| < 0.1\ {\rm m\,s^{-1}}$, Fig. 2a) as expected for shallow water surface gravity waves. The signal strength is typically $SS > 180$ counts (Fig. 2b), well above the suggested $\gamma_{\rm SS} = 100$ counts cutoff (Elgar et al. 2005). In addition, correlations generally are high > 0.8 (Fig. 2c), above the $\gamma_{\rm CORR} = 0.526$ (Eq. 1 with $f_s = 8$ Hz) cutoff (Elgar et al. 2001). However, occasionally the vertical velocities are quite large (exceeding $|w| > 0.8\ {\rm m\,s^{-1}}$). and noisy (*e.g.,* near 35 s in Fig. 2a) when SS (Fig. 2b) or CORR (Fig. 2c) are low, falling below the suggested $\gamma_{\rm SS}$ and $\gamma_{\rm CORR}$ cutoffs.

The SS has a minima at an apparent noise floor of 42 counts. CORR can fall below $\gamma_{\mathrm{CORR}} = 0.526$ when SS does not (*i.e.,* near 20 s in Fig. 2). For the entire data run, $\delta_{\mathrm{SS}} = 0.016$, exceeding the Elgar et al. (2005) $\delta_{\mathrm{SS}} = 0.008$ cutoff, which would result in rejection of this data run. The fraction of combined bad SS and CORR data points $\delta_{\mathrm{CORR}} = 0.045$, exceeding that typically observed by Raubenheimber et al. (2004) and Feddersen et al. (2007). It is not known whether this level of δ_{CORR} can be tolerated in estimating ϵ.

3. Quality Control (QC) of ADV Data

a. Signal Strength (SS) QC of Surfzone ADV Data

FIG. 3

Within a data run, ADV data is marked bad when the returned signal-strength $\mathrm{SS} < \gamma_{\mathrm{SS}}$ at any of the 3 acoustic beams with $\gamma_{\mathrm{SS}} = 100$ counts (Elgar et al. 2005). With a ≈ 42 count ADV noise floor (see Fig. 2b) and a 0.43 dB/count conversion, this $\gamma_{\mathrm{SS}} = 100$ count cutoff corresponds to a 25 dB cutoff, which is more conservative than the 15 dB Sontek (2004) recommendation. However, the resulting δ_{SS} is insensitive to γ_{SS} within the range of 80–130 counts (16-38 dB).

The fraction of bad SS data runs δ_{SS} is calculated for all the data runs. At all instruments, δ_{SS} did not systematically depend upon instrument height above the bed indicating that high levels of near-bed suspended sediment (Beach and Sternberg 1996, *e.g.,*) does not adversely impact ADV signal-strength. In the nearshore and surfzone, the sea-surface fluctuates due to infragravity and sea-swell surface gravity waves which can expose out of the water an instrument deployed below the mean surface. The amount the ADV transducer is exposed out of the water and thus δ_{SS} is expected to increase with smaller z'_{tr} (the distance of the downward-facing ADV transducer below the mean sea surface) and increase with larger significant wave amplitude a_{sig}. Reflecting this, δ_{SS} is inversely related to the normalized ADV transducer depth $z'_{\mathrm{tr}}/a_{\mathrm{sig}}$ (Fig. 3) with a consistent relationship that collapses at all surfzone instrument locations (1–4). At $z'_{\mathrm{tr}}/a_{\mathrm{sig}} = 0.5$, δ_{SS} varies

between 0.1–0.2, and for larger $z'_{\rm tr}/a_{\rm sig} \geq 1$ (conceptually, the ADV transducer below the significant trough level), $\delta_{\rm SS}$ is much reduced, generally < 0.02. If $a_{\rm sig}$ does not include infragravity fluctuations, the relationship between $\delta_{\rm SS}$ and $z'_{\rm tr}/a_{\rm sig}$ does not collapse as well, particularly near the shoreline (instrument 1) where infragravity energy can be significant (*e.g.,* Guza and Thornton 1985). Not all large $\delta_{\rm SS}$ result from ADV exposed out of the water. Occasionally $\delta_{\rm SS} = 0.1$ when $z'_{\rm tr}/a_{\rm sig} \approx 2$ (Fig. 3) and at times ($< 2\%$ of data runs) $\delta_{\rm SS} > 0.01$ at instruments 5 and 6, which are always well below the mean surface ($z'_{\rm tr}/a_{\rm sig} > 1.75, 2.75$, respectively; not shown). Other mechanisms (lack of sufficient scatterers or acoustic absorption/scattering) induce these moderate $\delta_{\rm SS}$. The Elgar et al. (2005) $\delta_{\rm SS} < 0.008$ criteria (horizontal dashed red line in Fig 3) rejects all data runs with $z'_{\rm tr}/a_{\rm sig} \lesssim 1$ which may be of particular interest for turbulence studies.

The functional form for the $\delta_{\rm SS}$–$z'_{\rm tr}/a_{\rm sig}$ relationship-boundary is approximately given by a quartic relationship,

$$\log_{10}(\delta_{\rm SS}) = -0.17(z'_{\rm tr}/a_{\rm sig} + c)^4 - 1.64(z'_{\rm tr}/a_{\rm sig} + c)^2 - 0.32, \tag{3}$$

where $c = 0.15$ (gray-dashed curve in Fig. 3). Although not aesthetically pleasing, the relationship (3) holds at all surfzone instruments regardless of whether in the swash-zone (lower tide at instrument 1) or surfzone. When designing surfzone ADV deployments, (3) yields a $\delta_{\rm SS}$ estimate for a downward facing ADV. For example, if a $\delta_{\rm SS} = 0.1$ is tolerable, then measurements potentially can be made as shallow as $z'_{\rm tr}/a_{\rm sig} = 0.48$. FIG. 4

For each data run, the bad SS data gaps are binned into probability density functions (pdf) of data gap-lengths from 1/8–60 s. The data gap-length statistics dependence upon $\delta_{\rm SS}$ is used to help determine criteria to reject data runs. The pdf maximum (the mode) is typically at or near 1/8 s (1 sample) for all $\delta_{\rm SS}$ (blue dots in Fig. 4). The gap-length means and standard deviations (std) increase with increasing $\delta_{\rm SS}$ (circles and asterisks in Fig. 4). At all $\delta_{\rm SS}$, the data gap length means and std are roughly equal, and together with a 1 point mode, suggests approximately exponentially distributed data gap-lengths. The data gap-length statistics dependence upon $\delta_{\rm SS}$ is independent of ADV location. For $\delta_{\rm SS} \leq 0.1$, both data gap-length mean and std are typically < 2 s, and are

linear with $\log_{10}(\delta_{\rm SS})$. For example, between the order of magnitude change from $\delta_{\rm SS} = 10^{-2}$ to $\delta_{\rm SS} = 10^{-1}$, the data gap-length mean and std only increase from approximately 1 to 2 seconds. For larger $\delta_{\rm SS}$ (> 0.1), the gap-length means and std increase rapidly, suggesting a different nature of exposure out of the water, and that such $\delta_{\rm SS}$ levels are not tolerable.

Bad SS data runs consistently out of the water are rejected with a $\delta_{\rm SS}$ cutoff $\delta^{\rm c}_{\rm SS}$ (*i.e.,* data runs with $\delta_{\rm SS} > \delta^{\rm c}_{\rm SS}$). A balance is sought in selecting $\delta^{\rm c}_{\rm SS}$ to retain data runs higher in the water column of interest for turbulence studies. At typical mid-surfzone locations (2 and 3), varying $\delta^{\rm c}_{\rm SS}$ from 0.008 (*e.g.,* Elgar et al. 2005) to 0.1 results in 1/3-1/2 more retained good-SS data runs with smaller $z'_{\rm tr}/a_{\rm sig}$. As the bad SS data-gap statistics are still small and increasing slowly (Fig. 4), the SS cutoff $\delta^{\rm c}_{\rm SS} = 0.1$ is chosen to retain more of the surfzone data runs within the range $0.6 < z'_{\rm tr}/a_{\rm sig} < 1.5$ (Fig. 3) that would otherwise be rejected. The impact of this choice is subsequently discussed.

b. Correlation (CORR) QC of Surfzone ADV Data

FIG. 5

After rejecting bad-SS ($\delta_{\rm SS} > 0.1$) data runs, the correlation (CORR) QC is applied to the remaining data runs. Data points with ${\rm CORR} < \gamma_{\rm CORR}$ on any of the 3 ADV beams are marked as bad, where $\gamma_{\rm CORR} = 0.562$ is given by (1) with $f_s = 8$ Hz (Elgar et al. 2005). Bad SS data points are also marked as bad CORR. The resulting fraction of total bad data points, denoted $\delta_{\rm CORR}$, can be significantly larger than $\delta_{\rm SS}$ (Fig. 5). Even for small $\delta_{\rm SS}$ ($< 10^{-3}$), $\delta_{\rm CORR}$ can approach one, reflecting the different processes leading to low signal-strength (exposure out of the water) and low correlation (Doppler noise or bubbles). Instruments 2, 3, and 4, had the strongest levels of wave breaking, consistently have the largest values of $\delta_{\rm CORR}$ relative to $\delta_{\rm SS}$ (see legend in Fig. 5). An alternative velocity QC algorithm ("despiking", Goring and Nikora 2002), that uses velocity signal properties together with a minimum CORR of 0.3, gives a similar fraction bad data points as $\delta_{\rm CORR}$.

FIG. 6

For examining $\delta_{\rm CORR}$ dependencies, the sensing volume vertical location ($z_{\rm adv}$ or $z'_{\rm adv}$), as

opposed $z_{\rm tr}$ is the appropriate vertical location as Doppler noise within the sensing volume lead to low correlations (*e.g.,* Lhermitte and Lemmin 1994). The $\delta_{\rm CORR}$ do not depend systematically upon the elevation of the sensing volume above the bed ($z_{\rm adv}$). Wave-breaking is a source of surfzone turbulence (George et al. 1994; Bryan et al. 2003; Feddersen and Trowbridge 2005) and bubbles (*e.g.,* Deane and Stokes 2002) to the upper water column. Thus, elevated $\delta_{\rm CORR}$ are expected higher up in the water column and under more intense breaking waves. The breaking-wave turbulence and bubble input rate depends upon the wave energy flux gradient $\mathrm{d}F/\mathrm{d}x$, where F is the cross-shore wave energy flux. The $\delta_{\rm CORR}$ relationship to $z'_{\rm adv}/a_{\rm sig}$ and $\mathrm{d}F/\mathrm{d}x$ are examined.

Assuming non-reflective, normally incident waves and integrating over the sea-swell band (0.05–0.3 Hz), the energy flux F is estimated at each instrument location solely from pressure via

$$F = g \int_{0.05\ \mathrm{Hz}}^{0.3\ \mathrm{Hz}} P_{\eta\eta}(f) c_g(f) \mathrm{d}f, \tag{4}$$

where g is the gravitation constant and c_g is the linear-theory group velocity. These wave energy flux estimates (4) are largely consistent with estimates derived from combined Pressure+ADV data that take into account non-normal wave incidence and reflection (Sheremet et al. 2005). However, the Pressure+ADV based F estimates are not independent of ADV data quality, and thus are not used. Wave energy flux gradients $\mathrm{d}F/\mathrm{d}x$ are estimated at instruments 1–5 by differencing F estimates from the neighboring onshore and offshore instruments. At location 1, $F = 0$ is assumed at the shoreline.

Considering only good-SS data runs, the relationship of $\delta_{\rm CORR}$ to $z'_{\rm adv}/a_{\rm sig}$ (Fig. 6a) is analogous to that for $\delta_{\rm SS}$ (Fig. 3) with $\delta_{\rm CORR}$ increasing with smaller $z'_{\rm adv}/a_{\rm sig}$. In contrast to the tighter $\delta_{\rm SS}$ relationship, the $\delta_{\rm CORR}$ range increases with $z'_{\rm adv}/a_{\rm sig}$. As $z'_{\rm adv}/a_{\rm sig} \to 1$, the data cloud becomes a nose and $\delta_{\rm CORR}$ approaches one (Fig. 6b). For any data runs with $z'_{\rm adv}/a_{\rm sig} \leq 1$, $\delta_{\rm CORR} > 0.7$ (not shown). Note that the non-dimensional instrument depths $z'_{\rm adv}/a_{\rm sig}$ are larger than $z'_{\rm tr}/a_{\rm sig}$ (Fig. 3) and are not directly comparable.

At fixed $z'_{\rm adv}/a_{\rm sig}$, $\delta_{\rm CORR}$ is generally larger with increasing $\mathrm{d}F/\mathrm{d}x$ (note the color stratification in Fig. 6), particularly for $1 < z'_{\rm adv}/a_{\rm sig} < 2.5$ (Fig. 6b). Non-dimensionalized surfzone

dissipation observations (*e.g.,* George et al. 1994) and bubbles (*e.g.,* Garret et al. 2000) decay with depth. The elevated δ_{CORR} closer to the surface and with stronger wave-breaking is consistent with small-scale turbulent- or bubble-induced Doppler noise within the sensing volume. Measurements closer to the bed (*e.g.,* $z'_{\mathrm{adv}}/a_{\mathrm{sig}} = 3$), even with large $\mathrm{d}F/\mathrm{d}x$ (red points in Fig. 6a), can have low δ_{CORR} ($< 10^{-3}$) as small-scale turbulence and bubbles are reduced farther below the surface. With the factors that affect δ_{CORR} understood, the dependence of the ϵ QC upon δ_{CORR} is examined next.

4. Quality Control of Turbulent Dissipation Rate ϵ

a. Calculation of ϵ

Turbulent dissipation rate ϵ is estimated from observed (high) frequency vertical velocity spectrum with the Lumley and Terray (1983) model that converts a wavenumber (k) spectrum $\hat{P}_{ww}(k)$ to to a frequency spectrum $P_{ww}(f)$ in a mixed wave and mean current environment. Variants of this method have been used to estimate nearshore ϵ (Trowbridge and Elgar 2001; Feddersen et al. 2007). A Kolmogoroff inertial subrange velocity wavenumber spectra $\hat{P}_{ww}(k) \sim \epsilon^{2/3}k^{-5/3}$ due to homogeneous isotropic turbulence (*e.g.,* Batchelor 1953) is assumed present. At frequencies higher than the wave frequencies, ϵ is derived from the observable $P_{ww}(f)$ through the model form (Lumley and Terray 1983; Trowbridge and Elgar 2001)

$$P_{ww}(f) = \frac{\alpha\epsilon^{2/3}}{2(2\pi)^{3/2}} M_{ww}(f; \bar{\mathbf{u}}, \sigma^2_{u,v,w}), \tag{5}$$

where $\alpha = 1.5$ is Kolmogoroff's constant, $\bar{\mathbf{u}}$ and $\sigma^2_{u,v,w}$ are the mean and (wave-dominated) variance of the 3 velocity components, and M_{ww} is an integral over 3D wavenumber space that transforms the inertial-subrange $k^{-5/3}$ wavenumber dependence to frequency (Trowbridge and Elgar 2001; Feddersen et al. 2007). For all non-pathological velocity mean and variances $M_{ww} \sim f^{-5/3}$ (Gerbi et al. 2009) meaning that, within an inertial-subrange, $P_{ww}(f) \sim f^{-5/3}$. As noise

levels are lower for the flow component parallel to the ADV orientation, the vertical (parallel to ADV body) velocity spectrum $P_{ww}(f)$ is used to estimate ϵ. Given the observed $P_{ww}(f)$ and estimated M_{ww}, the estimated $\epsilon(f)$ are calculated via (5).

Once bad SS and CORR data points are flagged, gap-free time series are generated in two ways to calculate velocity spectra. The first is "interpolation", following Elgar et al. (2005), resulting in a time series denoted by $w^{(\mathrm{i})}$. Data gaps $\leq$ 1 s long (8 data points) are linearly interpolated from the good data points bounding the gap. Bad data within the longer gaps is averaged together and the entire gap is set to this constant average value. The rationale is that velocity data noise is unbiased (as long as instrument is in the water) so that averaging the gap results in a more accurate mean current over the gap (Elgar et al. 2005). The interpolation method acts analogously to a low-pass filter biasing low the high-frequency spectra. The second method is "patching" (*e.g.,* $w^{(\mathrm{p})}$), which combines linear interpolation of short data gaps (≤ 0.5 s or 4 data points) and "patching together" of longer data gaps. Patching is illustrated with a discrete data sequence

$$w_k, w_{k+1}, w_{k+2}, \ldots, w_{k+m}, w_{k+m+1}$$

with a bad data gap of length m from indices $k+1$ to $k+m$. Patching cuts out the data from the gap and joins the good ends so that $w_{k+m+1} \rightarrow w_{k+1}$, reducing the time series length by the total number of bad data points. Patching has the potential for creating large steps in the resulting $w^{(\mathrm{p})}$ time series where the data gap ends are joined, which is expected to enhance (bias high) the high frequency spectrum. The interpolation of the shorter (and by far most common) gaps reduces the amount of time-shifting which would otherwise redistribute the spectrum's frequency distribution. Quantities (*i.e.,* spectra, ϵ) derived from patched and interpolated time series are denoted with "(p)" and "(i)" superscripts, respectively. Both patched and interpolated quantities are denoted with superscript "(p,i)".

Velocity spectra ($P_{uu}^{(\mathrm{p,i})}(f)$, $P_{vv}^{(\mathrm{p,i})}(f)$, and $P_{ww}^{(\mathrm{p,i})}(f)$) are calculated from the patched and interpolated time series using 70 sec long data-segments (detrended, Hanning windowed with 50% overlap) resulting in 88 degrees of freedom. At any frequency, the true spectrum is 95% likely to

be found within a factor of $[0.76, 1.38]$ of the observed spectrum. Analogously, $M_{ww}^{(\mathrm{p,i})}(f; \bar{\mathbf{u}}, \sigma_{u,v,w}^2)$ is estimated (see Feddersen et al. 2007) with the velocity mean and variance from the appropriate time series. Both $P_{ww}^{(\mathrm{p,i})}$ and $M_{ww}^{(\mathrm{p,i})}$, are only calculated for good-SS (*i.e.,* $\delta_{\mathrm{SS}} \leq 0.1$) data runs and that also pass a very broad criteria that $\delta_{\mathrm{CORR}} \leq 0.7$.

Both patched ($\epsilon^{(\mathrm{p})}(f)$ and interpolated ($\epsilon^{(\mathrm{i})}(f)$) dissipation are estimated at $N_f = 56$ frequencies between 1.2–2 Hz via

$$\epsilon^{(\mathrm{p,i})}(f) = \left[\frac{P_{ww}^{(\mathrm{p,i})}(f) 2(2\pi)^{3/2}}{\alpha M_{ww}^{(\mathrm{p,i})}(f; \bar{\mathbf{u}}, \sigma_{u,v,w}^2)} \right]^{3/2}. \tag{6}$$

This frequency range has been used previously (*e.g.,* Trowbridge and Elgar 2001; Feddersen et al. 2007) as little surface gravity wave variance is assumed present at these frequencies. Consistent with this assumption, a slope-break is often observed in velocity spectra (*e.g.,* near $f = 0.5$ Hz, Smyth and Hay 2003). If the model and inertial-subrange wavenumber spectrum are correct, then ϵ should be constant with f. At higher frequencies (> 3 Hz), P_{ww} generally has an approximately constant noise floor. Assuming no M_{ww} error induced by $\bar{\mathbf{u}}$ or $\sigma_{u,v,w}^2$ error, the P_{ww} spectra error bars result in the true $\epsilon^{(\mathrm{p,i})}(f)$ found within the interval $[0.66, 1.61]$ of the observed $\epsilon^{(\mathrm{p,i})}(f)$. Mean (frequency-averaged) dissipation rate $\bar{\epsilon}^{(\mathrm{p,i})}$ for the data run is calculated by averaging $\epsilon^{(\mathrm{p,i})}(f)$ over all frequencies. Alternative averaging methods, *i.e.,* $\bar{\epsilon} = \exp[\langle \log(\epsilon(f)) \rangle$ (Feddersen et al. 2007), result in negligible difference (typically 1%, always $< 5\%$) to standard-averaging. The $\bar{\epsilon}$ standard error $\varepsilon_{\bar{\epsilon}}$ is estimated from the variance of $\epsilon(f)$, *i.e.,* $\varepsilon_{\bar{\epsilon}}^2 = \mathrm{Var}[\epsilon(f)]/(N_f - 1)$. Note that the symbol ε is used to represent standard errors where the symbol ϵ is used to represent dissipation rate.

The resulting dissipation estimates $\bar{\epsilon}^{(\mathrm{p})}$ (and $\bar{\epsilon}^{(\mathrm{i})}$) range between $10^{-6}\ \mathrm{m^2\,s^{-3}}$ to $3 \times 10^{-3}\ \mathrm{m^2\,s^{-3}}$ and increases with δ_{CORR} (Fig. 7). Although the ratio $\sigma_{\bar{\epsilon}^{(\mathrm{p})}}/\bar{\epsilon}^{(\mathrm{p})}$ (varying between 0.03–0.06) is small, the $\bar{\epsilon}$ standard error does not indicate whether a data run $\bar{\epsilon}$ is consistent with an inertial subrange. The $\bar{\epsilon}^{(\mathrm{p,i})}$ increase with δ_{CORR} may be natural due to the more turbulent the surfzone the larger ϵ and also the larger δ_{CORR} . However, it is not apriori clear if $\bar{\epsilon}$ estimates at a particular δ_{CORR} are valid, and what δ_{CORR} level quality $\bar{\epsilon}$ estimates can be obtained. Additional quality control tests are applied to reject data runs inconsistent with an expected inertial-subrange.

FIG. 7

b. Example of P_{ww} and $\epsilon(f)$ frequency variability

FIG. 8

Examples of "interpolated" velocity spectra (*e.g.,* $P^{(\mathrm{i})}_{ww}(f)$) and frequency dependent dissipation ($\epsilon^{(\mathrm{i})}(f)$) from two data run at instrument 4 (with the most intense wave breaking and strongest currents) are shown in Fig. 8. In the first example (Fig. 8a), the $\delta_{\mathrm{CORR}} = 0.028$ is moderate, $H_{\mathrm{sig}}/h = 0.45$, indicative of the outer-surfzone, with observations relatively far ($z'_{\mathrm{adv}}/a_{\mathrm{sig}} = 3.32$) from the surface. The horizontal velocity spectra $P^{(\mathrm{i})}_{uu} + P^{(\mathrm{i})}_{vv}$ has a surface gravity wave peak (at $f = 0.07$ Hz), which falls off rapidly at intermediate-frequencies $0.3 < f < 0.7$ Hz, before encountering a slope-break at $f = 0.8$ Hz (red curve in Fig. 8a). At higher frequencies (0.8–3 Hz), $P^{(\mathrm{i})}_{ww}$ follows a power law with (between 1.2–2 Hz) best-fit exponent $\mu^{(\mathrm{i})}(\pm\varepsilon^{(\mathrm{i})}_{\mu}) = -1.74$ (± 0.12, where $\varepsilon^{(\mathrm{i})}_{\mu}$ is the standard error of $\mu^{(\mathrm{i})}$), close to the theoretical Kolmogoroff $\mu = -5/3$ inertial-subrange value (compare dashed green to thin blue curves in Fig. 8a). Consistent with the best-fit $\mu^{(\mathrm{i})}$ near $-5/3$, the estimated $\epsilon^{(\mathrm{i})}(f)$ are relatively constant in frequency (black curve in Fig. 8c). The mean dissipation $\bar{\epsilon}^{(\mathrm{i})} = 1.03 \times 10^{-4}\ \mathrm{m^2\,s^{-3}}$ (blue dashed line in Fig. 8c) and the best-fit slope of $\epsilon^{(\mathrm{i})}(f)$ with f, $-9.0 \times 10^{-6}\ \mathrm{m^2\,s^{-3}\,Hz^{-1}}$ (dotted line in Fig. 8c), is statistically indistinguishable from zero. The $\epsilon^{(\mathrm{i})}(f)$ 95% confidence limits (shaded gray region in Fig. 8c) also encompasses the $\bar{\epsilon}^{(\mathrm{i})}$ more than 95% of the time. The patched spectrum $P^{(\mathrm{p})}_{ww}$, power-law exponent $\mu^{(\mathrm{p})} = 1.75 \pm 0.11$, $\epsilon^{(\mathrm{p})}(f)$ slope ($= -9.4 \times 10^{-6}\ \mathrm{m^2\,s^{-3}\,Hz^{-1}}$), and $\bar{\epsilon}^{(\mathrm{p})} = 1.17 \times 10^{-4}\ \mathrm{m^2\,s^{-3}}$ are close to the respective interpolated quantities. That $\mu^{(\mathrm{p,i})}$ are near $-5/3$ suggests the presence of an inertial-subrange and a quality $\bar{\epsilon}$ estimate.

The second example has a larger $H_{\mathrm{sig}}/h = 0.55$ indicative of the inner-surfzone, measurements closer to the surface ($z'_{\mathrm{adv}}/a_{\mathrm{sig}} = 2.17$) and larger $\delta_{\mathrm{CORR}} = 0.255$ (Fig. 8b). Although the velocity spectra is consistent with pressure over the sea-swell band (*e.g.,* $\bar{\mathrm{C}}_{pu} = 0.91$), at higher (1–3 Hz) frequencies, $P^{(\mathrm{i})}_{uu} + P^{(\mathrm{i})}_{vv}$ is not monotonic (red curve in Fig. 8b) and the $P^{(\mathrm{i})}_{ww}$ spectra falls off too rapidly with frequency (power-slope of $\mu^{(\mathrm{i})} = -2.18 \pm 0.09$) for an inertial-subrange (compare blue to dashed-green curve in Fig. 8b). The patched $\mu^{(\mathrm{p})} = -2.13 \pm 0.13$ is similar to $\mu^{(\mathrm{i})}$. Consistent with $\mu^{(\mathrm{i})} \neq -5/3$, $\epsilon^{(\mathrm{i})}(f)$ is reduced with with increasing frequency. The

$\epsilon^{(\mathrm{i})}(f)$ best-fit slope, $-2.1 \times 10^{-4}\ \mathrm{m^2\,s^{-3}\,Hz^{-1}}$ (dotted line in Fig. 8d), is significantly different from zero. Note that the $\epsilon^{(\mathrm{i})}(f)$ error bars (shaded region in Fig. 8d) always encompass the $\bar{\epsilon}^{(\mathrm{i})} = 4.28 \times 10^{-4}\ \mathrm{m^2\,s^{-3}}$, indicating that this type of test to reject $\bar{\epsilon}$ estimates is insufficient. Furthermore, the patched and interpolated quantities are not consistent as $\bar{\epsilon}^{(\mathrm{p})}/\bar{\epsilon}^{(\mathrm{i})} = 1.82$, all together indicating that this data run is inconsistent with a turbulent inertial-subrange and that this $\bar{\epsilon}$ estimate should be rejected.

c. Application of ϵ QC Tests

Two independent QC tests, based upon the expected presence of an turbulent inertial-subrange, are applied to the patched and interpolated data runs and evaluated as a function of δ_{CORR}. Data runs that do not pass both tests are considered inconsistent with a turbulent inertial subrange and their $\bar{\epsilon}$ estimates are rejected. First, the $P_{ww}(f)$ power-law exponent μ is tested for consistency with $-5/3$. Second, a ratio of horizontal to vertical velocity spectra is required to be near one. These tests, examining the velocity spectra frequency variation and a bulk (frequency-integrated) quantity, are examined separately.

1) SPECTRA POWER-LAW EXPONENT CONSISTENT WITH AN INERTIAL SUBRANGE

FIG. 9

For each data run, the (patched and interpolated) best-fit exponents $\mu^{(\mathrm{p,i})}$ (with error bars $\pm\varepsilon_{\mu}^{(\mathrm{p,i})}$) are estimated by a least-squares fit of $\log(P_{ww}^{(\mathrm{p,i})})$ with $\log(f)$ over frequencies 1.2–2 Hz, as in the case examples (Fig. 8). fit standard error ($\varepsilon_{\mu}^{(\mathrm{p})}$ and $\varepsilon_{\mu}^{(\mathrm{i})}$) typically vary between 0.09 and 0.15. The estimated $\mu^{(\mathrm{p})}$ generally vary between -1 and -2.4 (dots in Fig. 9a), although the range spans $[-4, 0]$. At all δ_{CORR}, the $\mu^{(\mathrm{p})}$ binned-means are close to $-5/3$ (diamonds in Fig. 9a), suggesting that often an inertial-subrange is present and that the Lumley and Terray (1983) model for converting wavenumber to frequency spectra often is applicable at all δ_{CORR} levels. The $\mu^{(\mathrm{p})}$ binned-stds are generally near 0.35 and do not vary systematically with δ_{CORR} (vertical lines in Fig. 9a). At

$\delta_{\rm CORR} < 0.1$, the interpolated $\mu^{(\rm i)}$ and patched $\mu^{(\rm p)}$ are similar (Fig. 9b). At larger $\delta_{\rm CORR}$, the $\mu^{(\rm i)}$ binned-means are consistently $< -5/3$ and decrease with larger $\delta_{\rm CORR}$. These steeper spectral slopes are an artifact of the "interpolation" scheme which at higher $\delta_{\rm CORR}$ increasingly reduces high frequency energy (*i.e.,* is a low-pass filter).

The consistency of the estimated $\mu^{(\rm p)}$ and $\mu^{(\rm i)}$ with $-5/3$, as expected in an inertial-subrange in a wave-current environment (Gerbi et al. 2009), are tested to reject data runs. An analogous test examines whether the $\epsilon(f)$ best-fit slope with f is consistent with zero. Applying either test gives similar results, and as the μ test is more familiar (*e.g.,* Bryan et al. 2003; Jones and Monismith 2008) it is applied here. As the log-spectra are not Gaussian, the least-squares standard errors ε_μ are approximate, and rigorous statistical tests on $\mu^{(\rm p)}$ and $\mu^{(\rm i)}$ can not be applied. Instead, the quasi-heuristic criteria is used where a data run is rejected if the μ fit-skill < 0.5 or if the best-fit μ fall outside of the region

$$\mu - 2\varepsilon_\mu - \Delta < -5/3 < \mu + 2\varepsilon_\mu + \Delta, \tag{7}$$

where $\Delta = 0.06$. Allowing non-zero Δ gives the test (7) leeway given the uncertainty of the underlying distribution. If the μ estimates were Gaussian, then $\Delta = 0$ would correspond to 95% confidence limits and as typically $\varepsilon_\mu \approx 0.12$, $\Delta = 0.06$ corresponds to 99% confidence limits. In general the $\mu^{(\rm p,i)}$-fit skill was high. Only 1.3% and 0.8% of the patched and interpolated data runs, respectively, were rejected due to low skill. The first case example with $\mu^{(\rm i)} = -1.67 \pm 0.13$ (Fig. 8a) passes the test (7), whereas the second example with $\mu^{(\rm i)} = -2.14 \pm 0.09$ (Fig. 8b) fails. This criteria (7) is applied separately to all $\mu^{(\rm p)}$ and $\mu^{(\rm i)}$ for the good-SS data runs.

The good-$\mu^{(\rm p)}$ data runs (passing the test Eq. 7) generally fall within the range $-1.9 \leq \mu^{(\rm p)} \leq -1.4$ (Fig. 9c). The good-$\mu^{(\rm p)}$ binned-means are very close to $-5/3$ (diamonds in Fig. 9c), except for $\delta_{\rm CORR} > 0.4$, and the good-$\mu^{(\rm p)}$ binned-stds are reduced to around 0.14 (relative to 0.35 in Fig. 9a). For $\delta_{\rm CORR} > 0.2$, the fit-errors $\varepsilon_{\mu^{(\rm p)}}$ are approximately 50% larger than at smaller $\delta_{\rm CORR}$, allowing larger $\mu^{(\rm p)}$ deviation from $-5/3$ to pass the test (7). The $\mu^{(\rm i)}$ that pass (7) have a $\delta_{\rm CORR}$ dependence similar to $\mu^{(\rm p)}$ (compare Fig. 9d to 9c).

At various $\delta_{\rm CORR}$, between 50-80% of the good-SS data runs pass the $\mu^{(\rm p)}$-test (red triangles in Fig. 10). In total For $\delta_{\rm CORR} < 0.1$, the number N_μ of good-μ data runs is basically the same for patching and interpolation, although generally $N_\mu^{(\rm p)}$ is slightly greater than $N_\mu^{(\rm i)}$ (compare diamonds to triangles in Fig. 10). At $\delta_{\rm CORR} < 10^{-3}$, 80% of patched and interpolated data runs pass the μ test. Over all $\delta_{\rm CORR}$, 71% and 68% of patched and interpolated good-SS data runs pass the μ test. However, at larger $\delta_{\rm CORR}$ (> 0.1), $N_\mu^{(\rm i)}$ is more clearly reduced relative to $N_\mu^{(\rm p)}$ (compare diamonds to triangles in Fig. 10), as $\mu^{(\rm i)}$ are biased low (*i.e.,* Fig. 9b), and for binned $\delta_{\rm CORR} > 0.1$, the total $N_\mu^{(\rm p)}$ is 31% greater than the total $N_\mu^{(\rm i)}$,

FIG. 10

2) RATIO OF HORIZONTAL TO VERTICAL VELOCITIES CONSISTENT WITH AN INERTIAL SUBRANGE

FIG. 11

Although the power-law exponent μ test (7) rejects many data runs, some data runs pass with $\delta_{\rm CORR}$ as high as 0.6. To further test the data runs, the second $\bar{\epsilon}$ QC test examines the relationship between horizontal and vertical velocity spectra within an inertial subrange. Previously (Trowbridge and Elgar 2001; Feddersen et al. 2007), the estimated $\bar{\epsilon}$ reliability was determined by checking that the ratio $R \approx 1$, where R is based upon (2), and is defined as

$$R = \frac{(12/21)\langle f^{5/3}(P_{uu}(f) + P_{vv}(f) - \text{noise})\rangle}{\langle f^{5/3} P_{ww}(f)\rangle}, \tag{8}$$

where $\langle\rangle$ represents a frequency-average between 1.2–2 Hz, and "noise" is the $P_{uu} + P_{vv}$ ADV noise level averaged between 3.1–4 Hz. For all good-SS data runs, $R^{(\rm p)}$ and $R^{(\rm i)}$ are calculated via (8) from the patched and interpolated velocity spectra, respectively. Although $R = 1$ is not strictly required, as the assumptions that go into (2,8) are violated, the R dependence upon $\delta_{\rm CORR}$ is examined, and R limits are used to reject data runs inconsistent with an inertial-subrange.

First, consider the good-SS ($\delta_{\rm SS} < 0.1$) patched and interpolated data runs (Fig. 11a,b). For $\delta_{\rm CORR} < 10^{-2}$, both $R^{(\rm p)}$ and $R^{(\rm i)}$ are generally near one (binned-means between 0.9–1.2) but vary at fixed $\delta_{\rm CORR}$ with occasional outliers of $R^{(\rm p,i)} > 3$. For $\delta_{\rm CORR} < 10^{-1}$, $R^{(\rm p)}$ and $R^{(\rm i)}$

binned-means increase linearly with $\delta_{\rm CORR}$, the binned-std also increase, and generally $R^{(\rm p,i)} < 2$. At larger $\delta_{\rm CORR}$ (> 0.2), both $R^{(\rm p)}$ and $R^{(\rm i)}$ are typically > 2 and both binned-means and stds increase rapidly (Fig. 11a,b). Considering the subset of good-μ (that pass Eq. 7) data runs, the overall $R^{(\rm p)}$ and $R^{(\rm i)}$ dependence upon $\delta_{\rm CORR}$ (Fig. 11c,d) is qualitatively similar that for the good-SS data runs (Fig. 11a,b). The good-μ data runs removes many of the $R^{(\rm p,i)}$ outliers resulting in binned-means closer to one and much smaller binned-std. Thus the μ and R tests overlap, as both test for an inertial-subrange. At larger $\delta_{\rm CORR}$ (> 0.1), the good-μ $R^{(\rm p)}$ and $R^{(\rm i)}$ binned-means increase more slowly than the good-SS $R^{(\rm p,i)}$.

Although (2,8) are not strictly valid, that $R^{(\rm p)}$ and $R^{(\rm i)}$ are near one independently indicates that an inertial-subrange is often present. Based upon this, data runs are rejected which do not satisfy the heuristicly chosen criteria $0.5 < R^{(\rm p,i)} < 2$ (horizontal dashed lines in Fig. 11). For $\delta_{\rm CORR} < 0.1$, very few additional data runs are rejected with this test. At $\delta_{\rm CORR} > 0.2$, many $R^{(\rm p,i)} > 2$, outside of the selected heuristic range. For $\delta_{\rm CORR} > 0.1$, there are $1.5\times$ the number of good-μ-R patched versus interpolated data runs (235 versus 154) and the maximum $\delta_{\rm CORR} = 0.58$ and $\delta_{\rm CORR} = 0.34$ for patching and interpolation, respectively. Thus, at higher $\delta_{\rm CORR}$, patching is more often consistent with an inertial-subrange of turbulence and is preferable to interpolation.

5. Discussion

a. Ratio of $\bar{\epsilon}^{(\rm p)}/\bar{\epsilon}^{(\rm i)}$

The ratio $\bar{\epsilon}^{(\rm p)}/\bar{\epsilon}^{(\rm i)}$ dependence upon $\delta_{\rm CORR}$ is examined to determine their consistency. Ideally, the ratio $\bar{\epsilon}^{(\rm p)}/\bar{\epsilon}^{(\rm i)} = 1$. Considering all good-SS data runs, the ratio $\bar{\epsilon}^{(\rm p)}/\bar{\epsilon}^{(\rm i)}$ depends upon $\delta_{\rm CORR}$ (Fig. 12a) and generally $\bar{\epsilon}^{(\rm p)}/\bar{\epsilon}^{(\rm i)} \geq 1$, as expected. For $\delta_{\rm CORR} < 0.01$, the $\bar{\epsilon}^{(\rm p)}/\bar{\epsilon}^{(\rm i)}$ are near one (Fig. 12), and the choice of patching or interpolation does not impact $\bar{\epsilon}$. For $\delta_{\rm CORR} < 0.1$, the binned-mean $\bar{\epsilon}^{(\rm p)}/\bar{\epsilon}^{(\rm i)}$ slowly increase as does the scatter, but almost always $\bar{\epsilon}^{(\rm p)}/\bar{\epsilon}^{(\rm i)} < 1.5$. At

larger δ_{CORR} (> 0.2), the the binned-mean $\bar{\epsilon}^{(\mathrm{p})}/\bar{\epsilon}^{(\mathrm{i})}$ increases rapidly as does the scatter. For the subset of good-$\mu^{(\mathrm{p})}$-$R^{(\mathrm{p})}$ data runs, $\bar{\epsilon}^{(\mathrm{p})}/\bar{\epsilon}^{(\mathrm{i})}$ scatter is reduced (Fig. 12b) relative to only good-SS data runs (Fig. 12a). However, the trend of increasing $\bar{\epsilon}^{(\mathrm{p})}/\bar{\epsilon}^{(\mathrm{i})}$ at larger δ_{CORR} (> 0.1) is still present. For the good-$\mu^{(\mathrm{p})}$-$R^{(\mathrm{p})}$ data runs, deviations of $\bar{\epsilon}^{(\mathrm{p})}/\bar{\epsilon}^{(\mathrm{i})}$ from 1 are due to the effects of interpolation/averaging over longer gaps at higher δ_{CORR}. However, rarely is $\bar{\epsilon}^{(\mathrm{p})}/\bar{\epsilon}^{(\mathrm{i})} > 2$. As $\bar{\epsilon}$ typically varies over orders of magnitude (here almost 3 orders of magnitude), the factor of 2 difference between $\bar{\epsilon}^{(\mathrm{p})}$ and $\bar{\epsilon}^{(\mathrm{i})}$ further indicates that the good-SS-$\mu^{(\mathrm{p})}$-$R^{(\mathrm{p})}$ patched $\bar{\epsilon}^{(\mathrm{p})}$ are accurate.

FIG. 12

b. Relationship to the p-u Coherence Test

Previous surfzone ADV QC methodology (Elgar et al. 2001, 2005) were designed for wave and current studies (frequencies $\lesssim 0.2$ Hz), not for estimating $\bar{\epsilon}$ (frequencies between 1–2 Hz). For example, using a synchronized, co-located pressure measurement, Elgar et al. (2005) require that the sea-swell band spectral coherence ($\bar{\mathrm{C}}_{pu}$) between p and u is > 0.9, based upon the expectation that surfzone wave directional spread $< 25^{\circ}$. Although, many ADV based surfzone and air-sea boundary $\bar{\epsilon}$ studies did not have synchronized and co-located pressure measurements (Bryan et al. 2003; Feddersen et al. 2007; Jones and Monismith 2008; Gerbi et al. 2009), such measurements were made during HB06 and the relationship between $\bar{\mathrm{C}}_{pu}$ QC criteria and the inertial-subrange QC criteria is explored.

Here, $\bar{\mathrm{C}}_{pu}$ is calculated at all good-SS data runs as the sea-swell band average of the sea-surface elevation spectrum weighted cross-spectral p-u coherence C_{pu}, *i.e.,*

$$\bar{\mathrm{C}}_{pu} = \frac{\int_{0.05\ \mathrm{Hz}}^{0.3\ \mathrm{Hz}} \mathrm{C}_{pu}(f) P_{\eta\eta}(f) \mathrm{d}f}{\int_{0.05\ \mathrm{Hz}}^{0.3\ \mathrm{Hz}} P_{\eta\eta}(f) \mathrm{d}f}$$

where $\mathrm{C}_{pu}(f)$ is the spectral p-u coherence calculated with $u^{(i)}$, and $P_{\eta\eta}$ is the (depth-corrected) sea-surface elevation spectrum. For the good-SS data runs, $\bar{\mathrm{C}}_{pu}$ varies between 0.8–1.0 and is largely independent of δ_{CORR} (Fig. 13a). The $\bar{\mathrm{C}}_{pu} > 0.9$ test (dashed line in Fig. 13a) is failed by

33% of the good-SS data runs. The good-$\mu^{(\mathrm{p})}$-$R^{(\mathrm{p})}$ data runs have a similar $\bar{\mathrm{C}}_{pu}$ distribution with δ_{CORR} (Fig. 13b) to the good-SS data runs (Fig. 13a). The $\bar{\mathrm{C}}_{pu} > 0.9$ test is failed by 31% of these good-$\mu^{(\mathrm{p})}$-$R^{(\mathrm{p})}$ data runs. The bad-$\mu^{(\mathrm{p})}$-$R^{(\mathrm{p})}$ data runs also have a similar δ_{CORR} dependence and fail the $\bar{\mathrm{C}}_{pu} > 0.9$ test 34% of the time (not shown). Thus, the $\bar{\mathrm{C}}_{pu} > 0.9$ test is equally likely to pass or fail for both good and bad $\bar{\epsilon}^{(\mathrm{p})}$ estimates. This applies for other $\bar{\mathrm{C}}_{pu}$ thresholds from 0.8–1.0, demonstrating that the $\bar{\mathrm{C}}_{pu}$ test is not appropriate for quality controlling $\bar{\epsilon}$. FIG. 13

c. Vertical Distribution of Good Data Runs

FIG. 14

The vertical distribution of the remaining good data runs is examined to determine where in the water column $\bar{\epsilon}$ can be estimated. For all good-SS data runs, $\mu^{(\mathrm{p})}$ weakly decreases with smaller $z'_{\mathrm{adv}}/a_{\mathrm{sig}}$ (gray dots in Fig. 14a). However, the good-$\mu^{(\mathrm{p})}$ data runs (red dots in Fig. 14a), are independent of $z'_{\mathrm{adv}}/a_{\mathrm{sig}}$, consistent with absence of a good-$\mu^{(\mathrm{p})}$ and δ_{CORR} relationship (Fig. 9a,c). For all good-SS data runs, $R^{(\mathrm{p})}$ tends to one at larger $z'_{\mathrm{adv}}/a_{\mathrm{sig}}$, and $R^{(\mathrm{p})}$ generally increases with increased scatter at smaller $z'_{\mathrm{adv}}/a_{\mathrm{sig}}$ (Fig. 14b), consistent with the relationship between $R^{(\mathrm{p})}$ and δ_{CORR} (Fig. 11). The good-$\mu^{(\mathrm{p})}$ values of $R^{(\mathrm{p})}$ also follow this pattern with $z'_{\mathrm{adv}}/a_{\mathrm{sig}}$ (red dots in Fig. 14b). Between $1.2 < z'_{\mathrm{adv}}/a_{\mathrm{sig}} < 2$, about half of the good-$\mu^{(\mathrm{p})}$ data runs are additionally rejected by the $R^{(\mathrm{p})}$ limits. (Fig. 14b). At $z'_{\mathrm{adv}}/a_{\mathrm{sig}} > 2$ where most good-$\mu^{(\mathrm{p})}$-$R^{(\mathrm{p})}$ data runs are concentrated, the $R^{(\mathrm{p})}$ cutoff (dashed lines in Fig. 14b) reject only a few additional data runs. Although there are a few good-$\mu^{(\mathrm{p})}$-$R^{(\mathrm{p})}$ data runs as shallow as $z'_{\mathrm{adv}}/a_{\mathrm{sig}} = 1.2$, $\bar{\epsilon}^{(\mathrm{p})}$ can only be consistently estimated at $z'_{\mathrm{adv}}/a_{\mathrm{sig}} > 1.5$. When transformed from sensing-volume (z'_{adv}) to transducer (z'_{tr}) coordinates, this results in a limit of $z'_{\mathrm{tr}}/a_{\mathrm{sig}} > 1$, largely corresponding to a stricter SS cutoff of $\delta_{\mathrm{SS}} < 10^{-2}$ (Fig. 3), near the Elgar et al. (2005) cutoff of $\delta_{\mathrm{SS}} < 0.008$.

The vertical velocity power-law exponent μ has been observed to transition from near $-5/3$ to -1 within 0.1–0.15 m above the bed (Smyth and Hay 2003) as turbulent eddies become anisotropic. At $z_{\mathrm{adv}} \leq 0.1$ m (sensing volume within 0.1 m of the bed), the binned-mean $\mu^{(\mathrm{p})}$ deviates from $-5/3$ and approaches -1 (not shown). In addition, the $R^{(\mathrm{p})}$ values become larger,

consistent with anisotropic eddies. Few (22 out of 146, 15%) data runs passed both QC tests at $z_{\rm adv} < 0.1$. At $z_{\rm adv} > 0.1$ m, no change in $\mu^{(\rm p)}$ or $R^{(\rm p)}$ was observed. Thus $z_{\rm adv} = 0.1$ m is a lower near-bed limit on where $\bar{\epsilon}^{(\rm p)}$ can be estimated.

The $z'_{\rm adv}/a_{\rm sig} > 1.5$ limit is useful in designing an open-ocean air-sea boundary layer study (*e.g.,* Gerbi et al. 2009). The surfzone is a region of overlapping surface and bottom boundary layers, and from this alone the water column range where $\bar{\epsilon}^{(\rm p)}$ can be estimated is not clear. Within a saturated (self-similar) surfzone where $H_{\rm sig} = \gamma h$, where $\gamma \approx 0.5$ (Raubenheimber et al. 1996), the $z'_{\rm adv}/a_{\rm sig} \approx 1.5$ limit results in an water column limit of $z_{\rm adv}/h \lesssim 0.6$. Thus, turbulent dissipation rate ϵ can be consistently estimated in the lower 60% of the water column and more than 0.1 m above the bed within a saturated surfzone,

6. Summary

A quality control methodology for estimating surfzone turbulent dissipation rate ϵ from ADV observations is presented and applied to HB06 experiment data. First, ADV velocity measurements are quality controlled using the ADV backscattered signal-strength (SS) and correlation signal (CORR) to identify bad velocity data points. The fraction of bad SS data points $\delta_{\rm SS}$ increases inversely with the (wave-amplitude) normalized ADV transducer distance to the mean sea-surface, consistent with exposure out of the water as the dominant reason for bad SS. Based on statistics of the data-gap length, a liberal cutoff criteria of $\delta_{\rm SS} > 0.1$ is preliminarily chosen to reject data runs. The fraction of bad CORR data points $\delta_{\rm CORR}$ can be significant even when $\delta_{\rm SS}$ is small. The $\delta_{\rm CORR}$ is a function of both the (wave-amplitude) normalized ADV sensing volume distance below the mean sea-surface and also the wave-energy flux gradient, consistent with turbulence- and bubble-induced Doppler noise.

Turbulent dissipation rate $\bar{\epsilon}$ is estimated from vertical velocity spectra derived from both patched and interpolated time series. Two QC tests, based upon the properties of the expected turbulent inertial-subrange are applied to reject bad $\bar{\epsilon}$ data runs. The first test uses the vertical

velocity spectrum's power-law exponent μ, expected to be $-5/3$ in an inertial-subrange. The second test checks that a ratio R of horizontal and vertical velocity spectra band is consistent with an inertial subrange. For $\delta_{\rm CORR} < 0.1$, between 60-80% of patched and interpolated data runs pass these tests. At larger $\delta_{\rm CORR}$ (> 0.1), 50% more patched than interpolated data runs pass the tests, and patched data runs are used. Of the remaining data runs, the ratio of patched to interpolated dissipation $\bar{\epsilon}^{(\rm p)}/\bar{\epsilon}^{(\rm i)}$ is generally near one. Prior surfzone ADV QC methodologies designed for wave studies (frequencies $\lesssim 0.2$ Hz) have no predictive skill in rejecting bad $\bar{\epsilon}$ data runs. The resulting good $\bar{\epsilon}^{(\rm p)}$ data runs distributed at normalized vertical locations $z'_{\rm adv}/a_{\rm sig} > 1.5$. This suggests that turbulent dissipation rate can be consistently estimated over the lower 60% of the water column and > 0.1 m above the bed within a saturated (self-similar) surfzone.

Acknowledgements. The HB06 experiment and this research was supported by CA Coastal Conservancy, NOAA, ONR, NSF, and CA Sea Grant. R. T. Guza was co-PI on the HB06 experiment. Staff and students from the Integrative Oceanography Division (B. Woodward, B. Boyd, K. Smith, D. Darnell, I. Nagy, D. Clark, M. Omand, M. Yates, M. McKenna, M. Rippy, S. Henderson, and M. Spydell) were instrumental in acquiring the field observations for this research. In addition, R. T. Guza, Gerben Ruessink, G. Gerbi, and Peter Sutherland provided feedback on this work.

REFERENCES

Apotsos, A., B. Raubenheimer, S. Elgar, and R. T. Guza, 2008: Wave-driven setup and alongshore flows observed onshore of a submarine canyon. *J. Geophys. Res.*, **113**, doi:10.1029/2007JC004514.

Batchelor, G. K., 1953: *The Theory of Homogeneous Turbulence*. Cambridge University Press.

Beach, R. A., and R. W. Sternberg, 1996: Suspended-sediment transport in the surf zone: Response to breaking waves. *Cont. Shelf Res.*, **16**, 1989–2003.

Bryan, K. R., K. P. Black, and R. M. Gorman, 2003: Spectral estimates of dissipation rate within and near the surf zone. *J. Phys. Ocean.*, **33**, 979–993.

Cabrera, R., K. Deines, B. Brumley, and E. Terray, 1987: Development of a practical coherent acoustic Doppler current profiler. *Proc. Oceans '87*, IEEE Ocean Engineering Society, 93–97.

Clark, D. B., F. Feddersen, and R. T. Guza, 2010: Cross-shore surfzone tracer dispersion in an alongshore current. *J. Geophys. Res.*, revised.

Deane, G. B., and M. D. Stokes, 2002: Scale dependence of bubble creation mechanisms in breaking waves. *Nature*, **418**, 839–844.

Elgar, S., B. Raubenheimer, and R. T. Guza, 2001: Current meter performance in the surf zone. *J. Atmos. and Ocean. Tech.*, **18**, 1735–1746.

— 2005: Quality control of Acoustic Doppler Velocimeter data in the surfzone. *Measurement Science & Technology*, **16**, 1889–1893.

Feddersen, F., and J. H. Trowbridge, 2005: The effect of wave breaking on surf-zone turbulence and alongshore currents: a modelling study. *J. Phys. Ocean.*, **35**, 2187–2204.

Feddersen, F., J. H. Trowbridge, and A. J. Williams, 2007: Vertical structure of dissipation in the nearshore. *J. Phys. Ocean.*, **37**, 1764–1777.

Garret, C., M. Li, and D. Farmer, 2000: The connection between bubble size spectra and energy dissipation rates in the upper ocean. *J. Phys. Ocean.*, **30**, 2163–2171.

George, R., R. E. Flick, and R. T. Guza, 1994: Observations of turbulence in the surf zone. *J. Geophys. Res.*, **99**, 801–810.

Gerbi, G. P., J. H. Trowbridge, E. A. Terray, A. J. Plueddemann, and T. Kukulka, 2009: Observations of turbulence in the ocean surface boundary layer: energetics and transport. *J. Phys. Ocean.*, **39**, doi:10.1175/2008JPO4044.1, 1077–1096.

Goring, D. G., and V. I. Nikora, 2002: Despiking acoustic doppler velocimeter data. *Journal of Hydraulic Engineering*, **128**, 117–126.

Guza, R. T., and E. B. Thornton, 1980: Local and shoaled comparisons of sea surface elevations, pressures, and velocities. *J. Geophys. Res.*, **85**, 1524–1530.

— 1985: Observations of surf beat. *J. Geophys. Res.*, **90**, 3161–3172.

Jones, N. L., and S. G. Monismith, 2008: The influence of whitecapping waves on the vertical structure of turbulence in a shallow estuarine embayment. *J. Phys. Ocean.*, **38**, doi:10.1175/2007JPO3766.1, 1563–1580.

Kim, S., C. Friedrichs, J. Maa, and L. Wright, 2000: Estimating bottom stress in tidal boundary layer from Acoustic Doppler Velocimeter data. *J. Hydraul. Eng.-ASCE*, **126**, 399–406.

Lhermitte, R., and U. Lemmin, 1994: Open-channel flow and turbulence measurement by high-resolution doppler sonar. *J. Atmos. and Ocean. Tech.*, **11**, 1295–1308.

Lohrmann, A., R. Cabrera, and N. Kraus, 1994: Acoustic-Doppler velocimteter (ADV) for laboratory use. *Proc. Conf. on Fundamentals and Advancements in Hydraulic Measurements and Experimentation*, 351–365.

Lumley, J. L., and E. A. Terray, 1983: Kinematics of turbulence convected by a random wave

field. *J. Phys. Ocean.*, **13**, 2000–2007.

Martin, V., T. S. R. Fisher, R. G. Millar, and M. C. Quick, 2002: ADV data analysis for turbulent flows: Low correlation problem. *In: Hydraulic measurements and experimental methods 2002, Proc. of the specialty conference July 28 - August 1, 2002 Estes Park*.

Mori, N., T. Suzuki, and S. Kakuno, 2007: Noise of acoustic Doppler velocimeter data in bubbly flows. *Journal of Engineering Mechanics-ASCE*, **133**, doi:10.1061/(ASCE)0733-9399(2007)133:1(122), 122–125.

Omand, M. M., J. J. Leichter, P. J. S. Franks, A. J. Lucas, R. T. Guza, and F. Feddersen, 2010: Internal wave-driven patches of red tide in the nearshore and surfzone. *in preparation for Limnology and Oceanography*.

Raubenheimber, B., S. Elgar, and R. T. Guza, 1996: Wave transformation across the inner surf zone. *J. Geophys. Res.*, **101**, 25,589–25,597.

— 1998: Estimating wave heights from pressure measured in a sand bed. *J. Water. Port Coastal Ocean Eng.*, **124**, 151–154.

— 2004: Observations of swash zone velocities: A note on friction coefficients. *J. Geophys. Res.*, **109**, doi:10.1029/2003JC001877.

Scott, C. P., D. T. Cox, T. B. Maddux, and J. W. Long, 2005: Large-scale laboratory observations of turbulence on a fixed barred beach. *Measurement Science and Technology*, **16**, 1903–1912.

Sheremet, A., R. T. Guza, and T. H. C. Herbers, 2005: A new estimator for directional properties of nearshore waves. *J. Geophys. Res.*, **110**, doi:10.1029/2003JC002236.

Smyth, C., and A. Hay, 2003: Near-bed turbulence and bottom friction during SandyDuck97. *J. Geophys. Res.*, **108**, doi:10.1029/2001JC000952.

Sontek, 2004: *Sontek ADVField Acoustic Doppler Velocimeter: Technical Documentation*. Son-

tek/YSI, San Diego.

Spydell, M. S., F. Feddersen, and R. T. Guza, 2009: Observations of drifter dispersion in the surfzone: The effect of sheared alongshore currents. *J. Geophys. Res.*, **114**, doi:10.1029/2009JC005328.

Terray, E. A., M. A. Donelan, Y. C. Agrawal, W. M. Drennan, K. K. Kahma, A. J. Williams, P. A. Hwang, and S. A. Kitaigorodskii, 1996: Estimates of kinetic energy dissipation under breaking waves. *J. Phys. Ocean.*, **26**, 792–807.

Thomson, J., S. Elgar, T. H. C. Herbers, B. Raubenheimer, and R. T. Guza, 2007: Refraction and reflection of infragravity waves near submarine canyons. *J. Geophys. Res.*, **112**, doi:10.1029/2007JC004227.

Trowbridge, J., and S. Elgar, 2001: Turbulence measurements in the surf zone. *J. Phys. Ocean.*, **31**, 2403–2417.

Voulgaris, G., and J. H. Trowbridge, 2001: Evaluation of the Acoustic Doppler Velocimeter (ADV) for turbulence measurements. *Journal Atmospheric and Oceanic Technology*, **15**, 272–289.

Zedel, L., A. E. Hay, R. Cabrera, and A. Lohrmann, 1996: Performance of a single-beam pulse-to-pulse coherent Doppler profiler. *IEEE Journal of Oceanic Engineering*, **21**, doi:10.1109/48.508159, 290–297.

Generated with ametsocjmk.cls.
Written by J. M. Klymak
mailto:jklymak@ucsd.edu
http://opg1.ucsd.edu/ jklymak/WorkTools.html

Figure Captions

FIG. 1. HB06 cross-shore depth transect versus distance from the mean shoreline (blue curve). The instrumented frame locations are given by the circles and numbered 1–6. An additional instrumented frame, located between 1–2, was often buried, and is not considered here. The typical tide range is shown with the horizontal dashed red lines.

FIG. 2. Example ADV measured (a) vertical velocity w, (b) signal-strength (SS), and (c) correlation (CORR) versus time. This 160 s-long data segment is from instrument 1 (see Fig. 1) on 18 September 0500. The red dashed horizontal line in (b) is the suggested Elgar et al. (2005) cutoff. In (c) the correlation cutoffs (1) for $f_s = 8$ Hz ($\gamma_{\rm CORR} = 0.526$, red-dashed) and the mean flow $f_s = 0$ Hz ($\gamma_{\rm CORR} = 0.3$, magenta) are shown. The water depth $h = 0.57$ m, $H_{\rm sig} = 0.30$ m, $z_{\rm adv} = 0.13$ m, and $z'_{\rm tr} = 0.26$ m.

FIG. 3. Fraction of bad SS data points $\delta_{\rm SS}$ versus $z'_{\rm tr}/a_{\rm sig}$ at instruments 1–6 (see legend) where $z'_{\rm tr}$ is the distance of the ADV transducer below the mean sea surface and $a_{\rm sig}$ is the significant wave amplitude. Note that no instrument 6 data points are present in this axes range. The horizontal dashed-line is the $\delta_{\rm SS} = 8 \times 10^{-3}$ cutoff for discarding a data run (Elgar et al. 2005). The black-dashed curve is the proposed scaling (3) based upon the data.

FIG. 4. Mode, mean, and standard deviation of bad SS gap lengths versus $\delta_{\rm SS}$ at all instruments.

FIG. 5. δ_{CORR} versus δ_{SS} at all instruments (see legend). The vertical dashed line indicates the $\delta_{\mathrm{SS}} = 0.1$ cutoff.

FIG. 6. (a) The δ_{CORR} versus $z'_{\mathrm{adv}}/a_{\mathrm{sig}}$ at instruments 1–5 where $\log_{10}$ of the energy-flux gradient $\mathrm{d}F/\mathrm{d}x$ $(\mathrm{m}^3\,\mathrm{s}^{-3})$ is colored. Only good SS data runs that satisfy the $\delta_{\mathrm{SS}} \leq 0.1$ criteria are shown. Data runs with $\delta_{\mathrm{CORR}} > 0.7$ are not shown. Panel (b) is a blow up of the nose regions in panel (a).

FIG. 7. $\bar{\epsilon}^{(\mathrm{p})}$ versus δ_{CORR} for good-SS data runs at all instruments (see legend in Fig. 5).

FIG. 8. Example of vertical velocity spectra $P^{(i)}_{ww}(f)$ versus frequency f at instrument 3 that are (a) good (time = 240, $\delta_{\mathrm{CORR}} = 0.028$, $h = 1.83$ m, $H_{\mathrm{sig}} = 0.83$ m, $z'_{\mathrm{adv}}/a_{\mathrm{sig}} = 3.32$, and $\bar{\mathrm{C}}_{pu} = 0.86$ and (b) bad (time = 280, $\delta_{\mathrm{CORR}} = 0.255$, $h = 1.03$ m, $H_{\mathrm{sig}} = 0.57$ m, $z'_{\mathrm{adv}}/a_{\mathrm{sig}} = 2.17$, and $\bar{\mathrm{C}}_{pu} = 0.91$. The green dashed line is a -5/3 power slope. (c) and (d) are the $\epsilon^{(\mathrm{i})}(f)$ versus f over a narrower frequency range that correspond to (a) and (b). The solid black line is $\epsilon^{(\mathrm{i})}(f)$, the shaded region are the error bars (derived from $P^{(\mathrm{i})}_{ww}$) and the blue dashed line is $\bar{\epsilon}^{(\mathrm{i})}$ and the red dotted line is the linear best fit slope.

FIG. 9. Vertical velocity spectra P_{ww} power-law exponent (a) $\mu^{(\mathrm{p})}$ and (b) $\mu^{(\mathrm{i})}$ versus δ_{CORR} for all good SS data runs ($\delta_{\mathrm{SS}} < 0.1$). In (c) $\mu^{(\mathrm{p})}$ and (d) $\mu^{(\mathrm{i})}$ versus δ_{CORR} for cases that additionally also pass the $-5/3$-exponent test (7). The individual data points are represented as gray dots and the binned-means and stds are shown as diamonds and vertical bars, respectively. The horizontal dashed black line is the $-5/3$ slope. Note the change in vertical scale between (a,b) and (c,d).

FIG. 10. Binned number N of good-SS (N, circles), good-$\mu^{(\mathrm{p})}$ ($N_\mu^{(\mathrm{p})}$, red triangles), and good-$\mu^{(\mathrm{i})}$ ($N_\mu^{(\mathrm{i})}$, green diamonds) data runs versus δ_{CORR}.

FIG. 11. (a) $R^{(\mathrm{p})}$ and (b) $R^{(\mathrm{i})}$ versus δ_{CORR} at all instruments for the good SS ($\delta_{\mathrm{SS}} < 0.1$) data runs, and (c) $R^{(\mathrm{p})}$ and (d) $R^{(\mathrm{i})}$ versus δ_{CORR} for good-$\mu^{(\mathrm{p})}$ and good-$\mu^{(\mathrm{i})}$ data runs, respectively. Individual data points are represented as gray dots and the binned-means and stds are shown as diamonds and vertical bars, respectively. The dash-dot horizontal line represents $R = 1$. The horizontal dashed lines are the $R = 2$ and $R = 0.5$ cutoffs, respectively. Note the change in vertical scale between upper and lower panels.

FIG. 12. $\bar{\epsilon}^{(\mathrm{p})}/\bar{\epsilon}^{(\mathrm{i})}$ versus δ_{CORR} at all instruments for (a) good SS data runs ($\delta_{\mathrm{SS}} < 0.1$) and (b) good-$\mu^{(\mathrm{p})}$-$R^{(\mathrm{p})}$ data runs. The individual data points are represented as gray dots and the binned-means and stds are shown as diamonds and vertical bars, respectively.

FIG. 13. $\bar{\mathrm{C}}_{pu}$ versus δ_{CORR} at all instruments for (a) good-SS data runs ($\delta_{\mathrm{SS}} < 0.1$) and (b) good-$\mu^{(\mathrm{p})}$-$R^{(\mathrm{p})}$ data runs. The individual data points are represented as gray dots and the binned-means and stds are shown as diamonds and vertical bars, respectively. The dashed horizontal line at $\bar{\mathrm{C}}_{pu} = 0.9$ indicates the Elgar et al. (2005) cutoff.

FIG. 14. (a) $\mu^{(\mathrm{p})}$ and (b) $R^{(\mathrm{p})}$ versus $z'_{\mathrm{adv}}/a_{\mathrm{sig}}$. The good-SS data runs are in gray and the good-$\mu^{(\mathrm{p})}$ data runs are red. In (b), the dashed horizontal lines indicate the $R^{(\mathrm{p})}$ cutoffs.

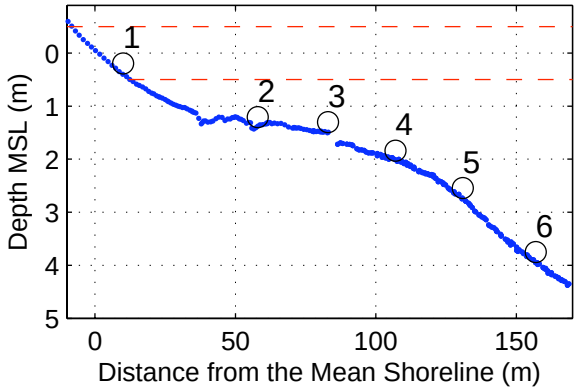

FIG. 1. HB06 cross-shore depth transect versus distance from the mean shoreline (blue curve). The instrumented frame locations are given by the circles and numbered 1–6. An additional instrumented frame, located between 1–2, was often buried, and is not considered here. The typical tide range is shown with the horizontal dashed red lines.

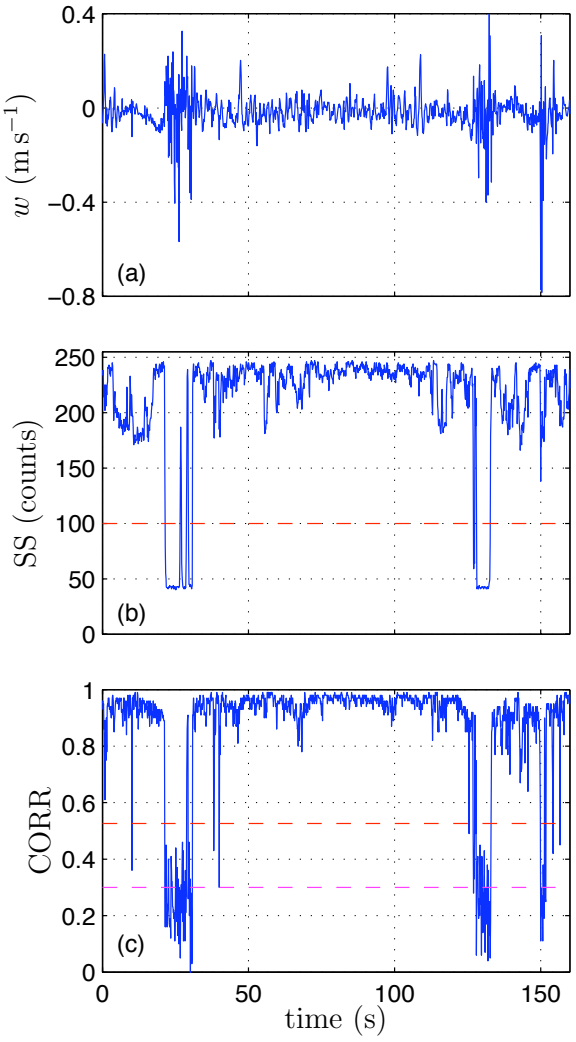

FIG. 2. Example ADV measured (a) vertical velocity w, (b) signal-strength (SS), and (c) correlation (CORR) versus time. This 160 s-long data segment is from instrument 1 (see Fig. 1) on 18 September 0500. The red dashed horizontal line in (b) is the suggested Elgar et al. (2005) cutoff. In (c) the correlation cutoffs (1) for $f_s = 8$ Hz ($\gamma_{\rm CORR} = 0.526$, red-dashed) and the mean flow $f_s = 0$ Hz ($\gamma_{\rm CORR} = 0.3$, magenta) are shown. The water depth $h = 0.57$ m, $H_{\rm sig} = 0.30$ m, $z_{\rm adv} = 0.13$ m, and $z'_{\rm tr} = 0.26$ m.

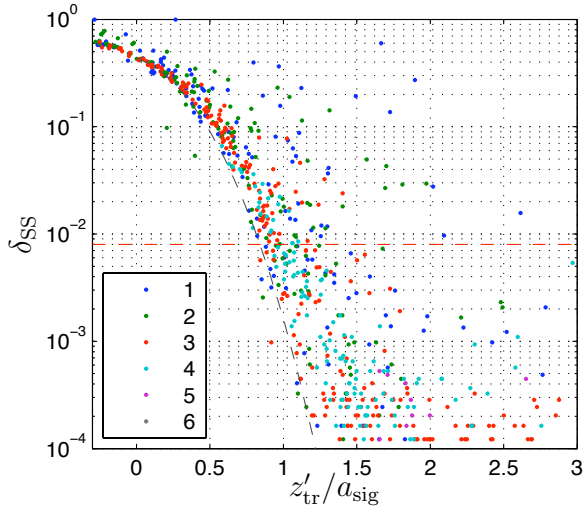

FIG. 3. Fraction of bad SS data points $\delta_{\rm SS}$ versus $z'_{\rm tr}/a_{\rm sig}$ at instruments 1–6 (see legend) where $z'_{\rm tr}$ is the distance of the ADV transducer below the mean sea surface and $a_{\rm sig}$ is the significant wave amplitude. Note that no instrument 6 data points are present in this axes range. The horizontal dashed-line is the $\delta_{\rm SS} = 8 \times 10^{-3}$ cutoff for discarding a data run (Elgar et al. 2005). The black-dashed curve is the proposed scaling (3) based upon the data.

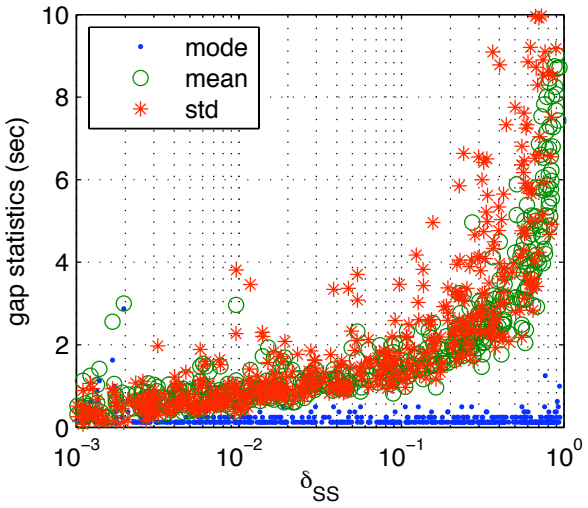

FIG. 4. Mode, mean, and standard deviation of bad SS gap lengths versus δ_{SS} at all instruments.

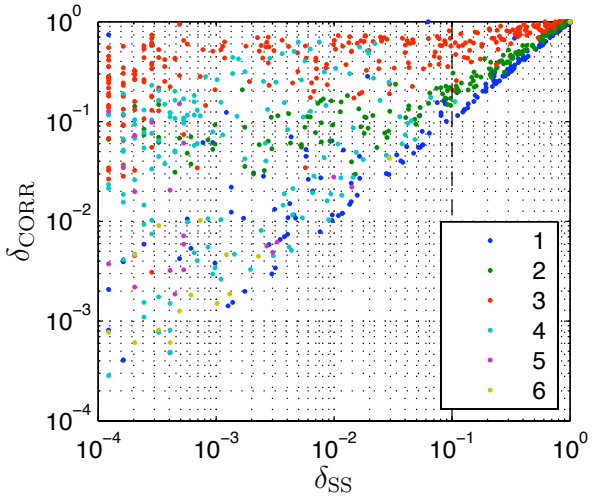

FIG. 5. δ_{CORR} versus δ_{SS} at all instruments (see legend). The vertical dashed line indicates the $\delta_{\mathrm{SS}} = 0.1$ cutoff.

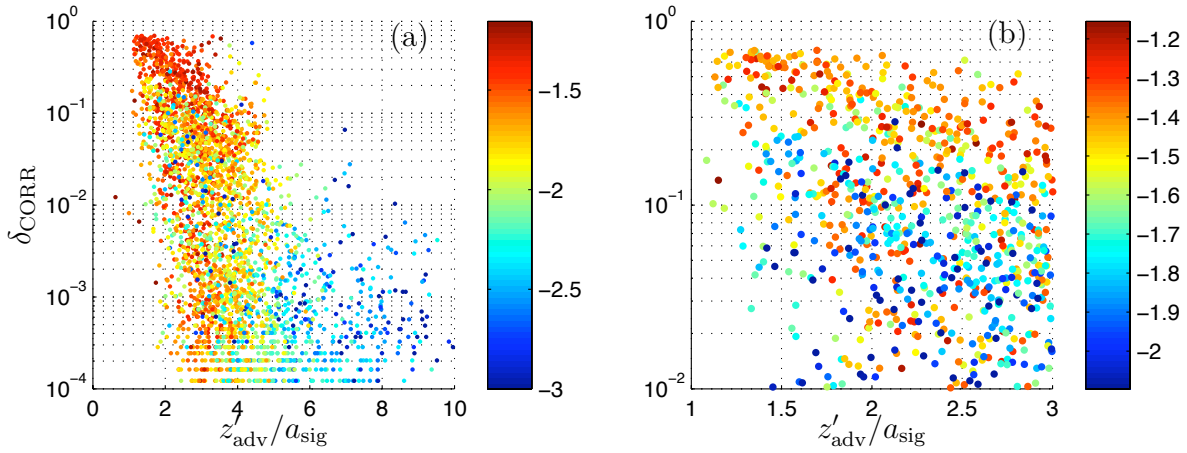

FIG. 6. (a) The δ_{CORR} versus $z'_{\mathrm{adv}}/a_{\mathrm{sig}}$ at instruments 1–5 where $\log_{10}$ of the energy-flux gradient $\mathrm{d}F/\mathrm{d}x$ $(\mathrm{m}^3\,\mathrm{s}^{-3})$ is colored. Only good SS data runs that satisfy the $\delta_{\mathrm{SS}} \leq 0.1$ criteria are shown. Data runs with $\delta_{\mathrm{CORR}} > 0.7$ are not shown. Panel (b) is a blow up of the nose regions in panel (a).

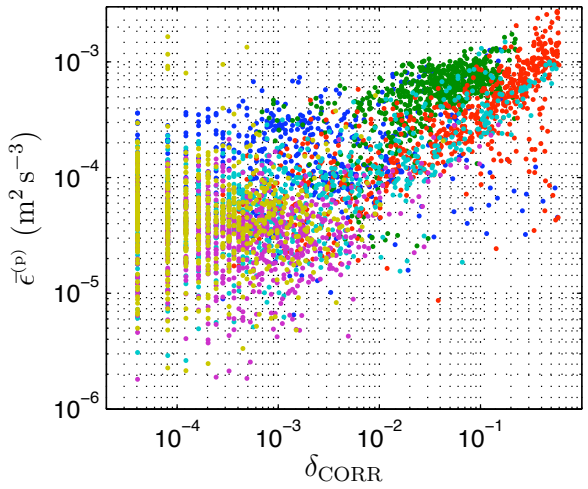

FIG. 7. $\bar{\epsilon}^{(\mathrm{p})}$ versus δ_{CORR} for good-SS data runs at all instruments (see legend in Fig. 5).

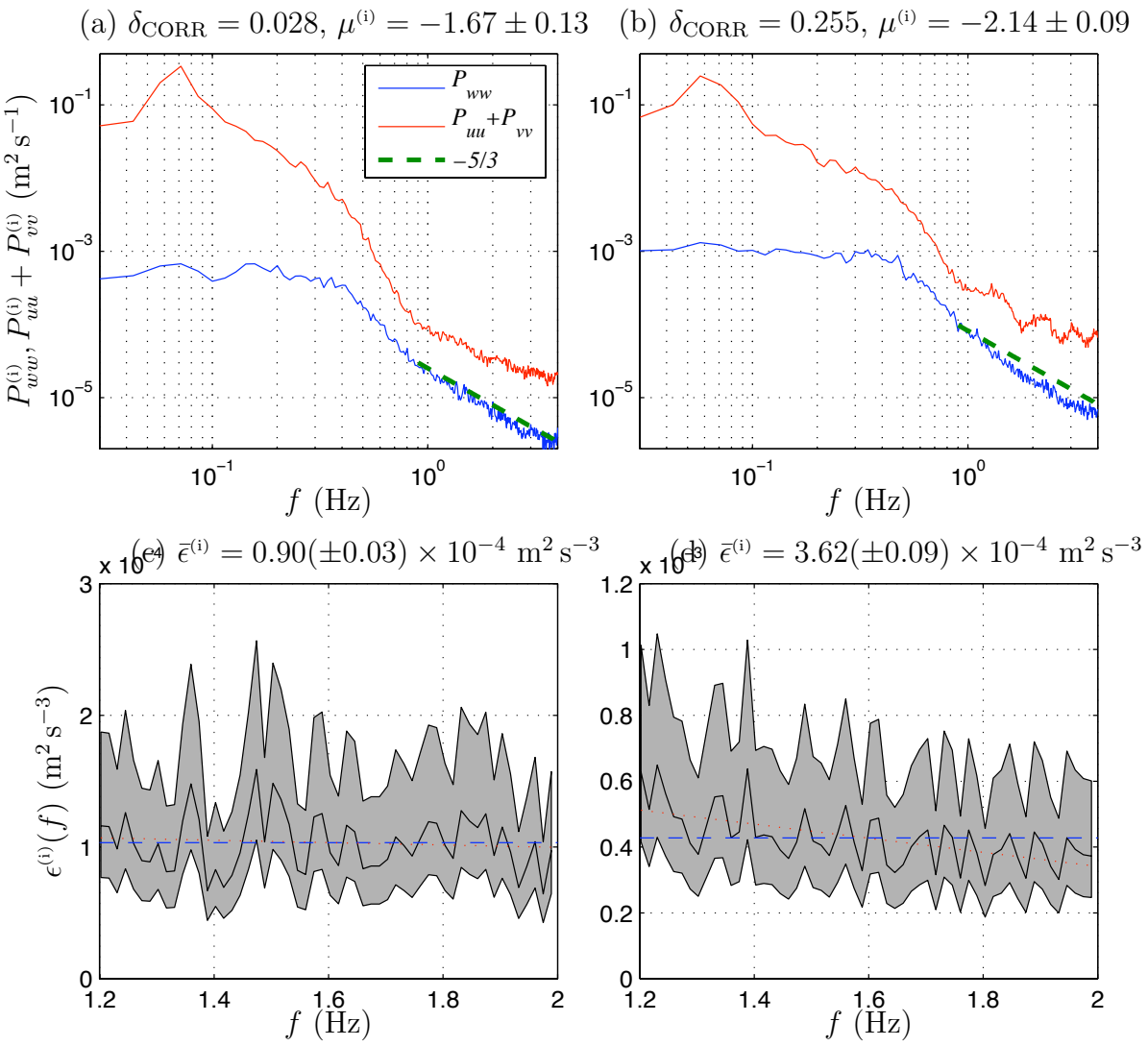

FIG. 8. Example of vertical velocity spectra $P^{(i)}_{ww}(f)$ versus frequency f at instrument 3 that are (a) good (time = 240, $\delta_{\rm CORR} = 0.028$, $h = 1.83$ m, $H_{\rm sig} = 0.83$ m, $z'_{\rm adv}/a_{\rm sig} = 3.32$, and $\bar{\rm C}_{pu} = 0.86$ and (b) bad (time = 280, $\delta_{\rm CORR} = 0.255$, $h = 1.03$ m, $H_{\rm sig} = 0.57$ m, $z'_{\rm adv}/a_{\rm sig} = 2.17$, and $\bar{\rm C}_{pu} = 0.91$. The green dashed line is a -5/3 power slope. (c) and (d) are the $\epsilon^{(\rm i)}(f)$ versus f over a narrower frequency range that correspond to (a) and (b). The solid black line is $\epsilon^{(\rm i)}(f)$, the shaded region are the error bars (derived from $P^{(\rm i)}_{ww}$) and the blue dashed line is $\bar{\epsilon}^{(\rm i)}$ and the red dotted line is the linear best fit slope.

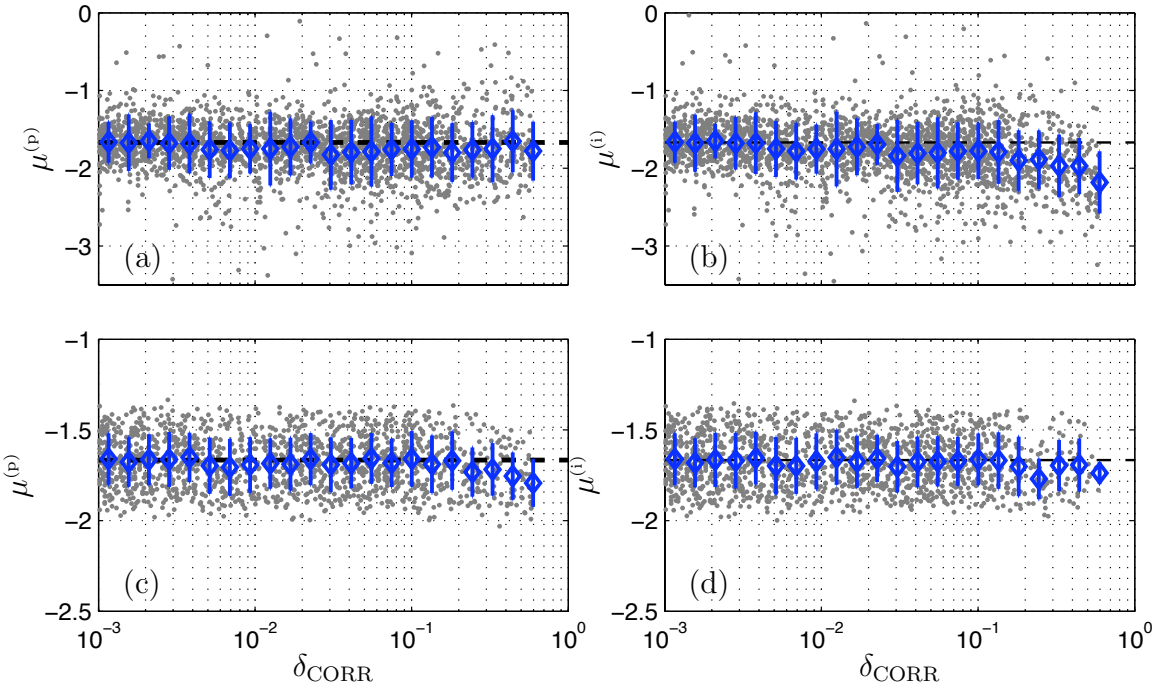

FIG. 9. Vertical velocity spectra P_{ww} power-law exponent (a) $\mu^{(\mathrm{p})}$ and (b) $\mu^{(\mathrm{i})}$ versus δ_{CORR} for all good SS data runs ($\delta_{\mathrm{SS}} < 0.1$). In (c) $\mu^{(\mathrm{p})}$ and (d) $\mu^{(\mathrm{i})}$ versus δ_{CORR} for cases that additionally also pass the $-5/3$-exponent test (7). The individual data points are represented as gray dots and the binned-means and stds are shown as diamonds and vertical bars, respectively. The horizontal dashed black line is the $-5/3$ slope. Note the change in vertical scale between (a,b) and (c,d).

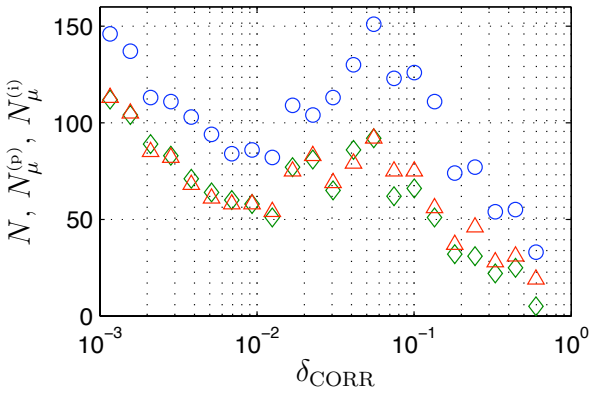

FIG. 10. Binned number N of good-SS (N, circles), good-$\mu^{(\mathrm{p})}$ ($N_\mu^{(\mathrm{p})}$, red triangles), and good-$\mu^{(\mathrm{i})}$ ($N_\mu^{(\mathrm{i})}$, green diamonds) data runs versus δ_{CORR}.

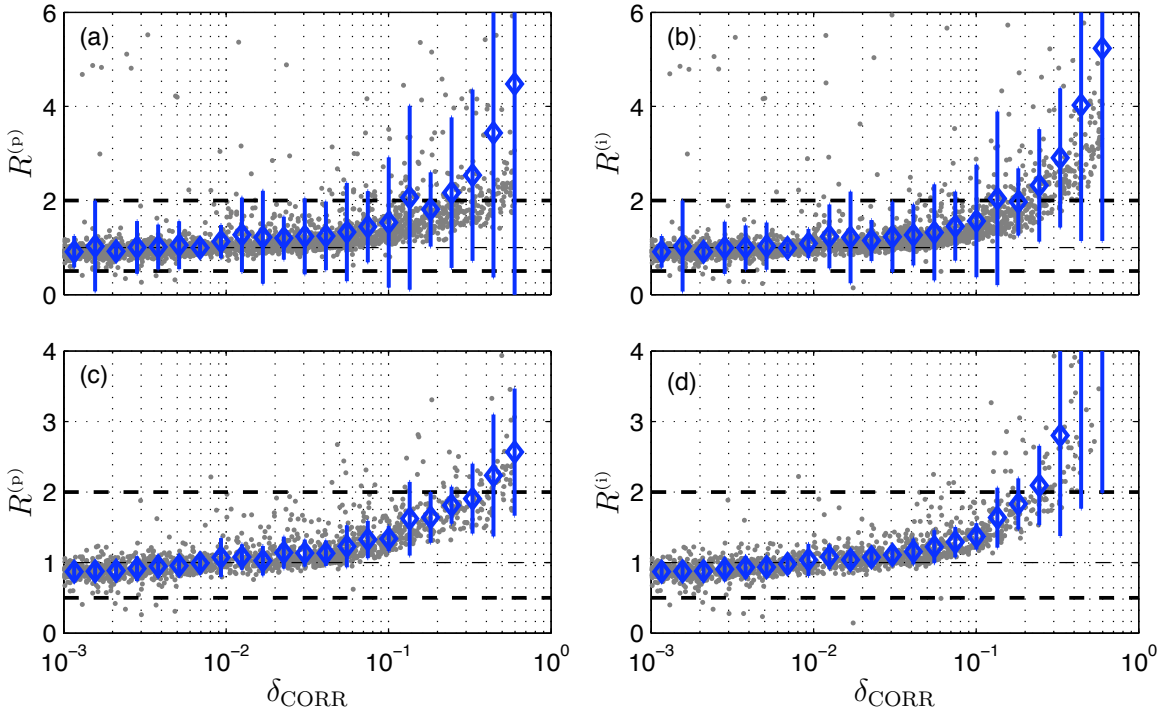

FIG. 11. (a) $R^{(\mathrm{p})}$ and (b) $R^{(\mathrm{i})}$ versus δ_{CORR} at all instruments for the good SS ($\delta_{\mathrm{SS}} < 0.1$) data runs, and (c) $R^{(\mathrm{p})}$ and (d) $R^{(\mathrm{i})}$ versus δ_{CORR} for good-$\mu^{(\mathrm{p})}$ and good-$\mu^{(\mathrm{i})}$ data runs, respectively. Individual data points are represented as gray dots and the binned-means and stds are shown as diamonds and vertical bars, respectively. The dash-dot horizontal line represents $R = 1$. The horizontal dashed lines are the $R = 2$ and $R = 0.5$ cutoffs, respectively. Note the change in vertical scale between upper and lower panels.

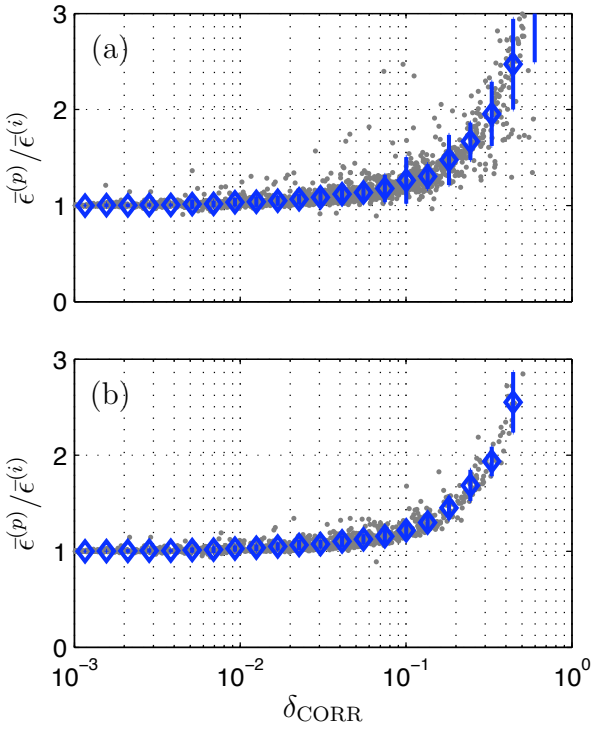

FIG. 12. $\bar{\epsilon}^{(\mathrm{p})}/\bar{\epsilon}^{(\mathrm{i})}$ versus δ_{CORR} at all instruments for (a) good SS data runs ($\delta_{\mathrm{SS}} < 0.1$) and (b) good-$\mu^{(\mathrm{p})}$-$R^{(\mathrm{p})}$ data runs. The individual data points are represented as gray dots and the binned-means and stds are shown as diamonds and vertical bars, respectively.

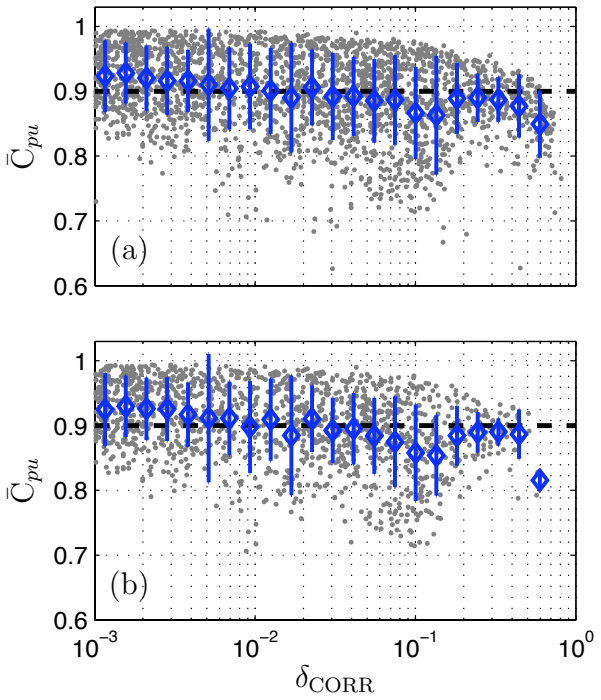

FIG. 13. $\bar{\mathrm{C}}_{pu}$ versus δ_{CORR} at all instruments for (a) good-SS data runs ($\delta_{\mathrm{SS}} < 0.1$) and (b) good-$\mu^{(\mathrm{p})}$-$R^{(\mathrm{p})}$ data runs. The individual data points are represented as gray dots and the binned-means and stds are shown as diamonds and vertical bars, respectively. The dashed horizontal line at $\bar{\mathrm{C}}_{pu} = 0.9$ indicates the Elgar et al. (2005) cutoff.

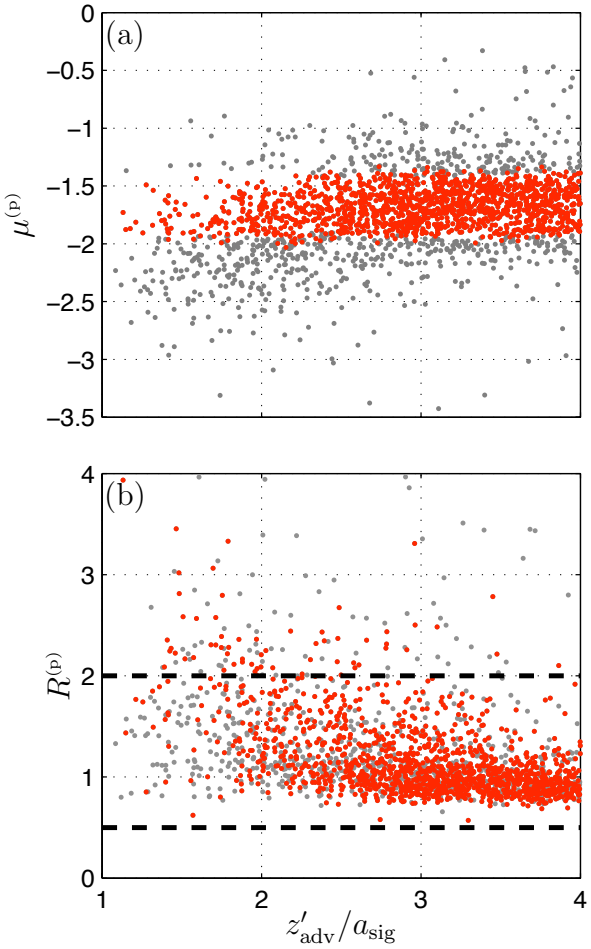

FIG. 14. (a) $\mu^{(\mathrm{p})}$ and (b) $R^{(\mathrm{p})}$ versus $z'_{\mathrm{adv}}/a_{\mathrm{sig}}$. The good-SS data runs are in gray and the good-$\mu^{(\mathrm{p})}$ data runs are red. In (b), the dashed horizontal lines indicate the $R^{(\mathrm{p})}$ cutoffs.